공학박사학위논문

LES 및 URANS를 이용한 원심펌프 내부의 난류 유동해석

Numerical investigation of turbulent flow in a centrifugal pump using LES and URANS

2021 년 8 월

서울대학교 대학원

기계항공공학부

계 범 준

LES 및 URANS를 이용한 원심펌프 내부의 난류 유동해석

Numerical investigation of turbulent flow in a centrifugal pump using LES and URANS

지도교수 최 해 천

이 논문을 공학박사 학위논문으로 제출함

2021년 4월

서울대학교 대학원

기계항공공공학부

계 범 준

계범준의 공학박사 학위논문을 인준함

2021년 6월

위 원 장 : 송 성 진

부위원장 : 최 해 천

위 원 : 황 원 태

위 원 : 이 창 훈

위 원 : 이 정 일

Numerical investigation of turbulent flow in a centrifugal pump using LES and URANS

Beomjun Kye
Department of Mechanical Engineering
Seoul National University

Abstract

Centrifugal pumps, which are the most common type of pumps, are widely used in various industrial applications. Centrifugal pumps often operate at off-design conditions as well as at the design condition to meet various ranges of pressure rise and flow rates required. At off-design conditions, more complex and unsteady flows develop inside pumps making an accurate prediction of the flow challenging. Commonly used Reynolds-averaged Navier-Stokes (RANS) turbulence model often inaccurately predict turbulent flow inside centrifugal pumps at off-design conditions. Therefore, more accurate numerical method like large eddy simulation (LES) is demanding.

In part I, we perform LES to investigate turbulent flow inside a volute-type centrifugal pump for the design and off-design condition. Along the pressure and suction sides of impeller blades, separation bubbles are generated. At the off-design condition, the blade pressure side near the tongue contains a larger separation bubble with highly unsteady characteristics due to the impeller-volute interaction. The trailing vortices shed from

rotating blades strongly interact with those from the following blade at the off-design condition, generating stronger vorticity field in a wider region inside the volute. On the other hand, this mutual interaction of vortices shed from consecutive blades is weak at the design condition. Triple decomposition of pressure fluctuations along the impeller periphery demonstrates that turbulent fluctuations are small at the design condition, whereas they become significant at the off-design condition especially near the tongue. Flow separation also occurs at the volute tongue. At the off-design condition, a large amount of volute flow does not follow the main stream to the discharge pipe but re-enters into the volute upstream near the tongue. This pressurized fluid forms a high adverse pressure gradient on the blade pressure side, resulting in strong unsteady separation there. Also, a high pressure gradient in the axial direction at the radial gaps is formed especially near the tongue, creating the leakage into the cavities. Inside the volute, secondary vortices grow along the volute passage. A secondary motion induced by these vortices also significantly affects the leakage to the cavities. All of these flow losses show unsteady features that are strongly influenced by impeller-volute interactions, especially at the off-design condition.

In part II, we conduct unsteady Reynolds-averaged Navier-Stokes (URANS) simulation and compare the flow characteristics with that by LES. URANS overpredicts the head coefficient and efficiency of the pump, whereas LES shows very good agreement with experiments. Vorticity fields inside the impeller and volute show that URANS does not resolve the instantaneous nature of turbulent flows. Rather, URANS displays similar magnitude and distribution of vorticity to phase-averaged fields by LES, indicating it provides phase-averaged flow features to some degree.

Inside the impeller passage, for the design condition, LES and URANS show similar characteristics for pressure and skin friction between five blades. On the other hand, along the blade pressure side for the off-design condition, LES reveals that higher pressure is induced near the tongue than the other four blades, delaying the reattachment of the separation bubble there. However, URANS does not show this larger separation bubble near the tongue. Along the impeller periphery, pressure fluctuations by LES and URANS are compared. For both flow conditions, URANS predicts periodic fluctuations well, whereas turbulent fluctuations are largely underestimated. Therefore, total fluctuations by LES and URANS exhibit satisfactory agreement at the design condition, whereas those at the off-design condition shows significant difference because of increased turbulent fluctuations for the latter condition. The time-averaged total pressure coefficient by LES and URANS shows good agreement at the design condition inside the volute. However, at the off-design condition, total pressure decreases at the volute upstream due to flow separation at the tongue. URANS does not predict these losses, overestimating total pressure there. Inside the discharge pipe for the present pump, strong flow separation and swirls are observed by LES due to the curvature and area expansion of the pipe. The losses by these swirls are larger for the design condition because of the higher mean flow rate. However, URANS does not capture strong swirls and subsequent losses, resulting in overprediction of the pressure rise and efficiency.

Keywords: centrifugal pump, large eddy simulation (LES), unsteady Reynolds Navier-Stokes equations (URANS), LES vs. URANS, impeller-volute interaction

Student number: 2015-22698

Contents

List of Figures

Part I Large eddy simulation of turbulent flow in a centrifugal pump

Part II LES vs. URANS: turbulent flow in a centrifugal pump

List of Tables

Part I.

Large eddy simulation of turbulent flow in a centrifugal pump

This part is based on "**Kye, B.**, Park, K., Choi, H, Lee, M, Kim, J.. 2018, *Int. J. Heat Fluid Flow*, Flow characteristics in a volute-type centrifugal pump using large eddy simulation".

Chapter 1

Introduction

A centrifugal pump, which is one of the most commonly used turbomachines, is widely utilized in residential buildings as well as in industries. In centrifugal pumps, the close interaction between the impeller and volute tongue causes complex three-dimensional flows, making numerical simulations challenging. centrifugal pumps often operate at various flow conditions as they are required to meet various ranges of pressure rise and flow rates. Therefore, understanding flow physics at off-design flow rates as well as the design flow rate is necessary to design better pumps. At off-design conditions, the flow characteristics inside centrifugal pumps become more complex than those at the design condition. Commonly used Reynolds-averaged Navier-Stokes (RANS) turbulence models often inaccurately predict the flow inside centrifugal pumps at off-design conditions (Byskov *et al.* 2003; Posa *et al.* 2011). For this reason, a large eddy simulation (LES) technique is a promising alternative to predict such complex flow phenomena inside centrifugal pumps.

Kato *et al.* (2003) performed LES to simulate the flow in a mixed-flow pump at various flow conditions, where the standard Smagorinsky model (Smagorinsky 1963) together with the van Driest damping function near the wall was used to model a subgrid-scale (SGS) stress tensor. The results from LES were compared with those measured by a laser Doppler velocimetry (LDV). LES predicted the phase-averaged meridional and tangential velocity accurately. Byskov *et al.* (2003) studied the flow in a shrouded six-bladed centrifugal pump impeller at design and off-design conditions using the localized dynamic Smagorinsky model (Piomelli & Liu 1995). They showed that, at an off-design condition, LES predicts complex flow phenomena, such as steady nonrotating stalls and flow asymmetry between impeller passages, better than RANS. Although most of previous LESs of flows in centrifugal pumps used the standard Smagorinsky model or simulated flow only in rotating parts, LESs using a more advanced subgrid-scale model such as a filtered structured function model (Posa *et al.* 2011) or a wall-adapting local eddy-viscosity model (Posa *et al.* 2015, 2016) were also performed to study turbulent flow in a centrifugal pump including all rotating and stationary parts. They showed that LES accurately predicts unsteady flow features, such as separated flow near the blade surfaces, back flow near the shroud surface and rotor-stator interaction, at design and off-design conditions. Feng *et al.* (2009*b*) performed a detached eddy simulation (DES) for the flow in a radial diffuser pump at low flow rates. The results from DES showed good agreements with those from particle image velocimetry experiments, capturing flow separation and back flows inside the impeller.

Although a number of successful LESs have been conducted to predict flow inside centrifugal pumps, LESs of the flow in volute-type centrifu-

gal pumps including both the impeller and volute casing have been fairly limited. Instead, RANS has been employed to investigate the impeller-volute interaction (González *et al.* 2002; Asuaje *et al.* 2005; Barrio *et al.* 2010; Cheah *et al.* 2011) and to improve the volute-type pump efficiency by optimizing the geometries of the impeller and volute (Barrio *et al.* 2008; Spence & Amaral-Teixeira 2009; Alemi *et al.* 2015). Volute-type centrifugal pumps, which operate without diffuser vanes, show complex flow features near the tongue due to direct interactions between the impeller and volute tongue. Recently, Zhang *et al.* (2016) performed an LES using a commercial software to analyze the flow in a volute-type centrifugal pump, where the standard Smagorinsky model was used as a subgrid-scale model. They reported that the impeller-volute interaction is dominated by vortex shedding in the wake of the blade trailing edge and pressure pulsations are strongly associated with the corresponding vorticity magnitude inside the pump. However, detailed flow features such as flow separation, leakage flow, trailing vortices shed from rotating blades and impeller-volute interaction inside the volute-type centrifugal pump have not been fully investigated. Thus, in the present study, we perform an LES of flow in a volute-type centrifugal pump including both the impeller and volute casing to understand the flow characteristics. The flow characteristics and losses at the off-design condition as well as the design condition will be discussed.

Chapter 2

Numerical details

2.1. Pump specifications and operating conditions

The pump under consideration is a 4kW commercial in-line circulation pump (Dooch DP 50-34/2) which is employed to circulate water for a heating and cooling system of buildings. The pump is a volute-type centrifugal pump (without diffuser vanes), and is comprised of a shrouded impeller with five backswept blades and a surrounding volute casing. Fig. 2.1 shows the two-dimensional views of the pump, where the blade position angle φ is defined by the azimuthal angle from the volute tongue to the trailing edge of the preceding blade suction side. We include the cavities between the impeller and volute to examine the leakage flow through radial gaps.

The pump specifications and operating conditions are summarized in table 2.1. The present centrifugal impeller is driven by an induction motor, and the rotational speed varies from 361 to 371 rad/s depending on the flow rate. Because the difference in the rotational speed over flow conditions is small (less than 3%) and it is known the dynamic similarity

is little affected by rotational speeds of pumps (Dixon & Hall 2014), we fix the rotational speed of the impeller Ω at 367 rad/s (i.e., 3500 rpm) and consider both design and off-design conditions (the difference in Reynolds numbers between experiments and simulations are less than 2%). The Reynolds number of the pump is $Re = 1,740,000$ based on the radius of the impeller blade R_2 and blade tip velocity U_2. To compare numerical results with experimental data measured at various rotational speeds, we compute the non-dimensional parameters such as the flow coefficient ϕ, head coefficient ψ, and efficiency η:

$$\phi = \frac{Q}{2\pi R_2 b_2 U_2}, \quad \psi = \frac{\Delta P_t}{0.5\rho U_2^2}, \quad \eta = \frac{\Delta P_t Q}{T\Omega} \tag{2.1}$$

where Q is the flow rate, b_2 is the impeller outlet width, ρ is the water density, ΔP_t is the total pressure rise of the pump, and T is the torque on the impeller.

2.2. Governing equations and computational setup

We solve the spatially filtered continuity and Navier-Stokes equations in a non-inertial reference frame that rotates with the centrifugal impeller (Fig. 2.2). The Navier-Stokes equations in this rotating frame are formulated in a strongly conservative form (Beddhu *et al.* 1996), and all variables are normalized by the impeller radius R_2 and the blade tip speed U_2:

$$\nabla \cdot \tilde{\mathbf{u}} - q = 0 \tag{2.2}$$

$$\frac{\partial \tilde{\mathbf{u}}}{\partial t} + \nabla \cdot \left[\left(\tilde{\mathbf{u}} - \mathbf{v} \right) \tilde{\mathbf{u}} + \tilde{\mathbf{u}} \mathbf{v} \right] = -\nabla \tilde{p} + \frac{1}{Re} \nabla^2 \tilde{\mathbf{u}} - \nabla \cdot \boldsymbol{\tau} + \mathbf{f} \tag{2.3}$$

where $\mathbf{u} = \mathbf{w} + \mathbf{v} = \mathbb{R}^{\mathsf{T}} \mathbf{u}_a$, $\mathbf{v} = \boldsymbol{\Omega} \times \mathbf{x}$. $\mathbf{u}$, $\mathbf{w}$, and $\mathbf{x}$ are the absolute velocity, relative velocity, and position vectors in the cylindrical coordinates

with the non-inertial reference frame, respectively. $\mathbf{u}_a$ is the absolute velocity vectors in the inertial reference frame, $\mathbb{R}$ is the rotational matrix. $\mathbf{\Omega}$, t, and p are the angular velocity of the impeller, time, and pressure, respectively. q and $\mathbf{f}$ are the mass source/sink and momentum forcing to meet the no-slip boundary condition and mass conservation for the cell containing the immersed boundary in the non-inertial frame, respectively (Kim & Choi 2006). The detailed procedure for determining q and $\mathbf{f}$ is given in Kim *et al.* (2001). The tilde $(\tilde{\cdot})$ indicates a spatial filter, and $\boldsymbol{\tau} = \widetilde{\mathbf{u}\mathbf{u}} - \tilde{\mathbf{u}}\tilde{\mathbf{u}}$ is the subgrid-scale (SGS) stress tensor. As in Kumar & Mahesh (2017), an approximation of $\widetilde{\mathbf{u}\mathbf{v}} = \tilde{\mathbf{u}}\mathbf{v}$ in the non-inertial frame is used. We adopt a dynamic global model for the SGS stress tensor (Park *et al.* 2006; Lee *et al.* 2010). The model coefficient, which is volume-averaged, is determined dynamically without any *ad hoc* clipping.

In the present study, we adopt the non-inertial frame of reference which is fixed to the rotating impeller. Thus, the boundary layers near the impeller surfaces are resolved more accurately because the grid nodes on and near the impeller are fixed in time. On the other hand, the volute casing and discharge pipe rotate in the opposite direction of the impeller rotation. This makes grid nodes for momentum forcing and mass source/sink be updated at every computational time step (but the grids do not change in time because of the use of IB method).

For the time advancement, the computational domain is decomposed into the inner and outer regions in the radial direction. The interface location is $r/R_2 = 0.72$ at which $r\Delta\theta/\Delta r$ (the ratio of circumferential to radial grid spacing) is about 1. For each region, a second-order semi-implicit fractional step method is applied (Akselvoll & Moin 1996): the azimuthal derivative terms in the inner region and radial derivative terms in

the outer region are integrated in time with the Crank-Nicolson method, while other derivatives in the inner and outer regions are integrated with a third-order Runge-Kutta method. All the spatial derivative terms are discretized by the second-order central difference scheme in a staggered grid. The same numerical method was applied to turbulent flows in an axial fan (Park *et al.* 2019) and a volute-type centrifugal pump (Kye *et al.* 2018).

The computational domain ranges $-0.36 \leqslant x/R_2 \leqslant 1.74$, $r/R_2 \leqslant 6$, and $0 \leqslant \theta \leqslant 2\pi$ in the axial, radial, and azimuthal directions, respectively. The origin of the computational domain is defined at the center of the impeller inlet (Fig. 2.1(a)). A top-hat velocity profile with a constant flow rate ($\phi_{\mathrm{d}} = 0.0845$ and $\phi_{\mathrm{off}} = 0.0483$ for the design and off-design conditions, respectively) is provided at the duct inlet ($x/R_2 = -0.36$, $r/R_2 \leqslant 0.51$), and the reference pressure is defined at the center of the duct inlet ($x/R_2 = -0.36$, $r/R_2 = 0$). The Neumann boundary condition is applied at the lateral boundary ($r/R_2 = 6$). $\mathbf{u} = \boldsymbol{\Omega} \times \mathbf{x}$ and $\mathbf{u} = 0$ are enforced with the immersed boundary method on the rotating and stationary surfaces, respectively.

2.3. Resolution studies and comparison to experiments

For a grid convergence test, we use four grid systems, where the finest mesh has approximately 512 million grid points (table 2.2). Fig. 2.3 describes the axial and radial grid distributions of LES3 (we use uniform grids in the azimuthal direction). In the axial direction, dense grids are placed in the impeller and discharge pipe, while the grid spacing in the radial direction is smallest at the location of the volute tongue where strong impeller-volute interaction occurs. The smallest axial and radial

grid spacings are $\Delta x/R_2 = \Delta r/R_2 = 0.002$. Between the blade tips, 284 grid points are assigned in the azimuthal direction. In the radial direction, 40 grid points are allocated between the blade tip and volute tongue. Further description on the grid systems was given in our earlier work (Kye *et al.* 2018).

To initialize flow fields of LES2 - LES4, solution of LES1 at $tU_2/R_2 = 54\pi$ (corresponding to 27 impeller revolutions) is used. Simulation with LES3 is then performed with a constant CFL (Courant–Friedrichs–Lewy) number of 1.2 until $tU_2/R_2 = 16\pi$ (corresponding to 8 impeller revolutions), and is further continued at a constant time step size of $\Delta tU_2/R_2 = \pi/1500$ (corresponding to 3,000 time steps per impeller rotation) to collect turbulence statistics. For the LES3 grids, 512 processors (Intel Xeon Phi 7250) at the KISTI supercomputing center are utilized for MPI parallel computations.

To verify the simulation results, experiments are conducted on a test rig as shown in Fig. 2.4(a). The experiments followed the international standard ISO 9906 and Korean standard KS B 6301 which describe procedures to evaluate performance of centrifugal pumps. The flow rate, pressure rise, torque, and efficiency of the pump are measured in experiments to obtain the non-dimensional performance parameters. Note that the experimental setup has an in-line layout where the inlet and outlet pipes keep a straight line, and the pump is installed between them. However, in the numerical simulation, the inflow is induced through the straight pipe below the impeller. The wear-ring clearance is also not included in the present simulation, and thus there is zero leakage from the bottom cavity (front chamber) to the pump inlet. Barrio *et al.* (2008) considered a volute-type centrifugal pump with a non-dimensional specific speed of

$\omega_s = \Omega\sqrt{Q}/(gH)^{0.75} = 0.47$, and reported that about 4% of the flow rate passed through the wear-ring clearance at the design condition. Although Zhang *et al.* (2016) ($\omega_s = 0.358$) reported considerable leakage (about 10% of the flow rate) through the wear-ring clearance, we expect that the present centrifugal pump ($\omega_s = 0.5$) is more analogous to the pump studied by Barrio *et al.* (2008) and thus the effect of leakage through the wear-ring clearance is less severe than that of Zhang *et al.* (2016). Zero leakage configuration for simulation of turbulent flow in centrifugal pumps are also considered in other previous studies (Barrio *et al.* 2010; Stel *et al.* 2013; González *et al.* 2006; Kato *et al.* 2003; Posa *et al.* 2016).

Fig. 2.4(b) shows the head coefficient and efficiency from LES at the design and off-desgin conditions ($\phi_{\mathrm{d}} = 0.0845$ and $\phi_{\mathrm{off}} = 0.0483$, respectively), together with those by experiments. Two performance parameter of LES converge to experimental ones with increasing grid resolution. The agreements of the pump performances by LES are excellent even for the off-design condition. With LES3, differences in two parameters are less than 1% for the design condition. At the off-design condition, the differences in the head coefficient and efficiency are about 1% and 4%, respectively. Since the pump performances by LES3 are nearly the same as those by LES4, we present the results from LES3 in the following.

Number of blades, N_b	5
Rotational speed, Ω	367 rad/s
Impeller inlet radius, R_1	32.5 mm
Impeller outlet radius, R_2	69 mm
Volute base circle radius, R_3	75 mm
Impeller outlet width, b_2	10.5 mm
Discharge pipe diameter, D_pipe	50 mm
Blade tip speed, U_2	25.3 m/s
Reynolds number, Re	1,740,000
Design flow coefficient, ϕ_d	0.0845
Off-design flow coefficient, ϕ_off	0.0483
Dimensionless specific speed, ω_s	0.5

Table 2.1: Pump specifications and operating conditions

	$N_x \times N_r \times N_\theta$
LES1	$193 \times 433 \times 768$
LES2	$257 \times 481 \times 1024$
LES3	$257 \times 641 \times 1536$
LES4	$385 \times 769 \times 1728$

Table 2.2: Grid systems of numerical simulations

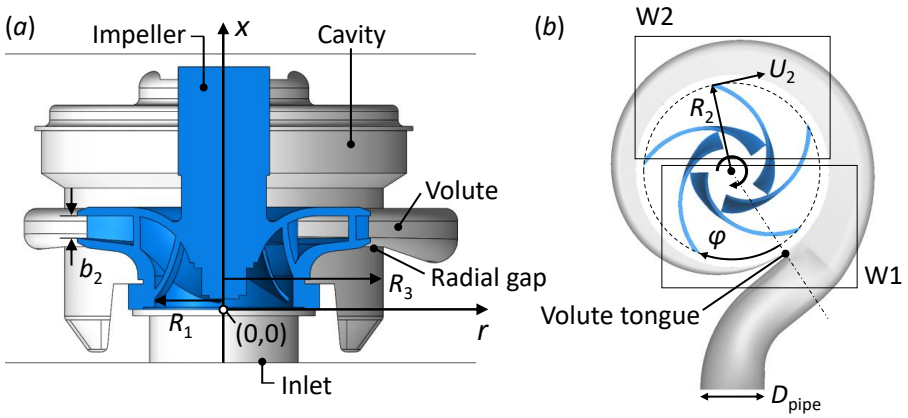

Figure 2.1: Schematic diagram of the impeller and volute casing: (a) front view; (b) top view ($\varphi = 54°$). The windows W1 and W2 represent specific regions of our interest.

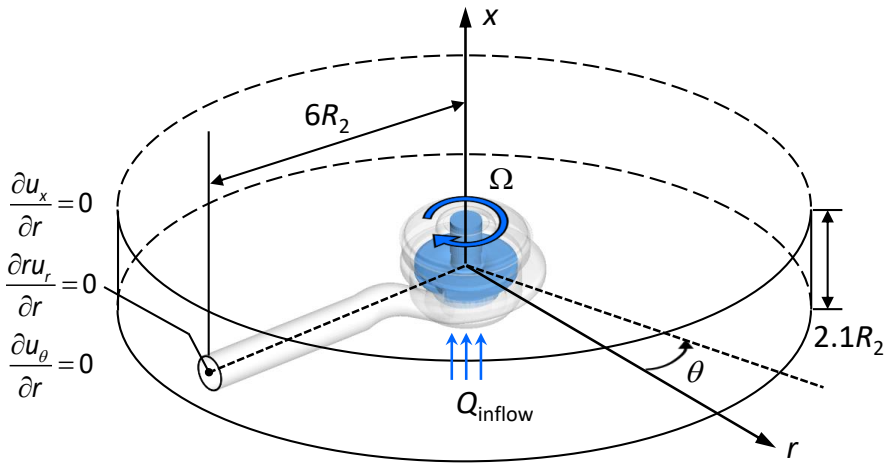

Figure 2.2: Schematic diagram of the coordinates, computational domain, and boundary conditions

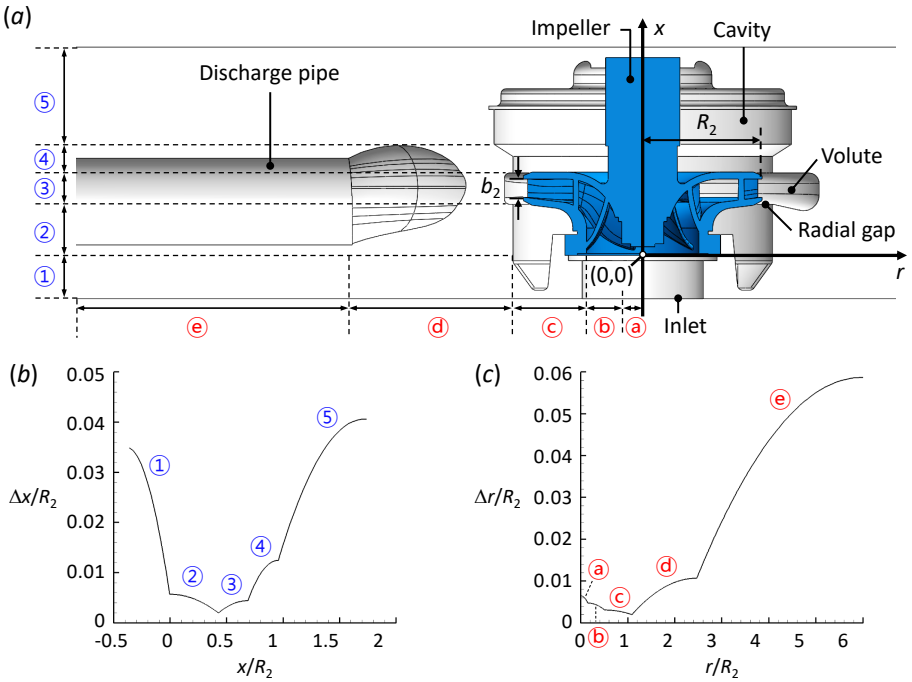

Figure 2.3: The grid distribution of LES3: (a) side view of the pump; (b) axial grid spacing; (c) radial grid spacing

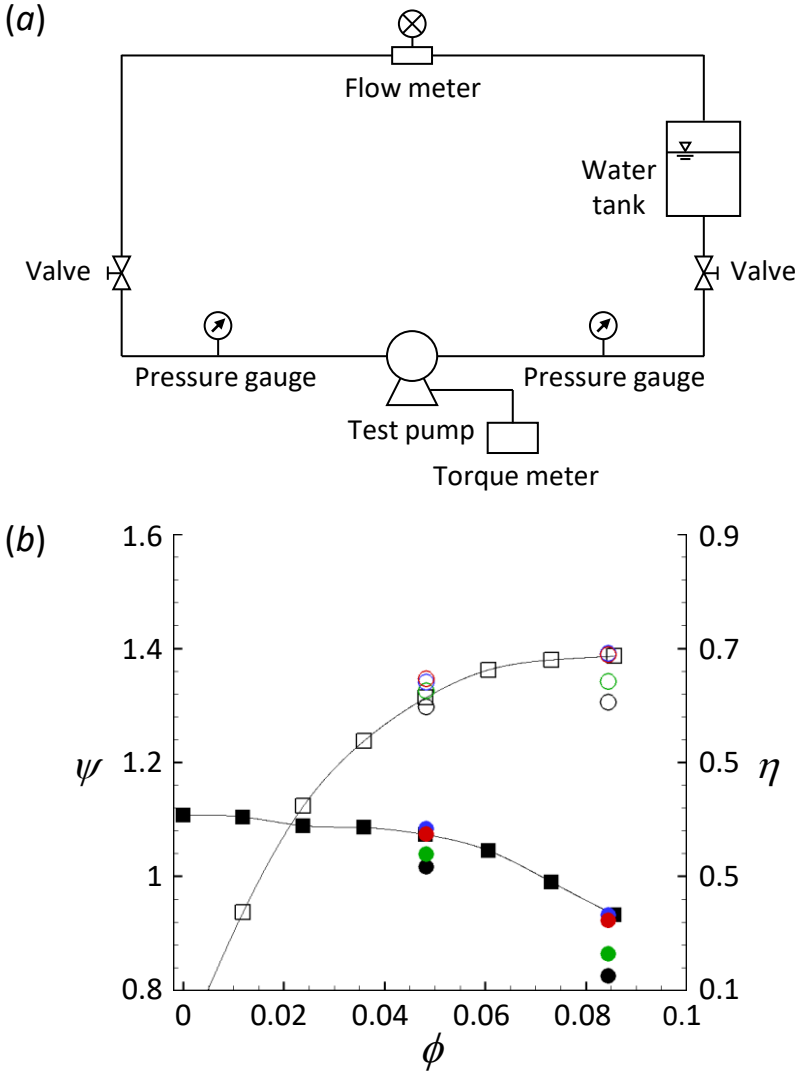

Figure 2.4: Experimental setup and performance curves: (a) schematic diagram of a pump test rig; (b) pump performances versus flow coefficient: (□, ■) experiments; (○, ●) LES1; (○, ●) LES2; (○, ●) LES3; (○, ●) LES4. In (b), solid and open symbols denote the head coefficient and efficiency, respectively.

Chapter 3

Results and discussions

3.1. Overall flow structures in a centrifugal pump

To understand the overall flow features in a centrifugal pump, we explore instantaneous three dimensional streamlines together with the pressure coefficient inside the impeller passage in Fig. 3.1. The pressure coefficient is defined by:

$$C_p = \frac{p - p_\infty}{0.5\rho U_2^2} \tag{3.1}$$

where p_∞ is defined at the center of the duct inlet ($x/R_2 = -0.36$, $r = 0$). Owing to the centrifugal acceleration driven by the impeller rotation, pressure increases rapidly inside the impeller passage. This relatively large pressure increase allows centrifugal pumps to be widely used to transport fluid for various applications. However, depending on the pressure gradient inside the passage, flow separation can occur as shown along the pressure side of the blade. The pressure rise is higher at the off-design condition (lower flow rate) because of the characteristics of backward-swept impeller blades than that at the design condition. The relative streamlines look similar but recirculation zones on the blade pressure side is larger at

the off-design condition than those at the design condition.

Figure 3.2 shows instantaneous streamlines together with the constours of pressure coefficient at the volute mid-span. Fluid discharged from the impeller flows through the volute and exits to the curved discharge pipe. Pressure further increases in the volute but the increment is not as large as in the impeller. At the design condition, the pressure rise inside the volute is moderate. On the other hand, at the off-design condition which has lower flow rate, the pressure increases rapidly because area expansion in the volute is larger than outflow from the impeller. This rapid pressure rise at the off-design flow rate inside the volute induces leakage through the radial gap between the impeller and tongue, which causes strong interaction between the impeller blade and volute tongue (Kye *et al.* 2018). This strong blade-tongue interaction for the off-design condition generates highly unsteady flow structures near the tongue like leakage, flow separation, and pressure fluctuations. These will be further discussed throughout this paper.

Figure 3.3 shows the instantaneous vortical structures at the design and off-design conditions. At both conditions, vortical structures develop from the leading edge of the blade suction side (denoted as α in this figure) and grow along the blade suction side. Vortices also develop from the leading edge of the blade pressure side (β), and interact with those developed from the suction side. These vortices travel over the separation bubble, and exit from the blade suction side. Unlike these vortices, vortical structures are hardly found inside the separation bubble on the blade pressure side. Vortices are also shed from the blade trailing edge (γ), and they interact with the volute tongue when they pass, creating strong vortices there (δ). At the off-design condition, the incidence angle

of flow becomes small at the impeller inlet and vortices from the leading edge of the blade pressure side (β) grow weaker. Also, vortical structures along the blade suction surface becomes weaker than those at the design condition because of lower flow rate (but the rotational speed is same to that of design condition; see Table 2.1) at the off-design condition. Nevertheless, the vortices along the volute and near the tongue are much stronger at the off-design condition than those at the design condition due to stronger impeller-volute interaction for the former case. Unlike for the design condition (about 14% of ϕ_{d}), about 26% of the flow rate (ϕ_{off}) goes through the gap between the impeller and volute tongue (leakage; Barrio *et al.* 2010) at the off-design condition, which causes strong interaction between the impeller blade and volute tongue.

3.2. The flow characteristics inside the impeller

3.2.1. *Relative eddy and equations of motion in a non-inertial frame*

Before analyzing the flow characteristics inside the impeller, we explain the concepts of the relative eddy and reduced pressure which are helpful to understand impeller flows. The relationship between the absolute vorticity and the vorticity observed in the non-inertial reference frame is provided as follows (Greitzer *et al.* 2004):

$$\boldsymbol{\omega} = \boldsymbol{\omega}_{\mathrm{rel}} + 2\boldsymbol{\Omega}. \tag{3.2}$$

where $\boldsymbol{\omega}$ and $\boldsymbol{\omega}_{\mathrm{rel}}$ designate absolute and relative vorticity, respectively. In general, absolute vorticity of the inflow to the impeller is assumed to be small. Thus, in the non-inertial coordinate system, flow rotating in the direction opposite to the impeller's rotation is induced inside the impeller, which is called the relative eddy. Thus, flow in an impeller is accelerated

along the blade suction side and decelerated along the blade pressure side by the relative eddy. A similar explanation was also given in literature (Greitzer *et al.* 2004; Dixon & Hall 2014).

Next, we consider the momentum equations for incompressible flows in the non-inertial frame of reference (Kim & Choi 2006):

$$\left.\frac{D\mathbf{w}}{Dt}\right|_n = -\nabla p + \frac{1}{Re}\nabla^2\mathbf{w} - \mathbf{\Omega}\times(\mathbf{\Omega}\times\mathbf{r}) - 2\mathbf{\Omega}\times\mathbf{w} \tag{3.3}$$

Equation 3.3 represents momentum equations with source terms in the non-inertial reference frame. All variables are non-dimensionalized by the characteristic velocity and length scales. For the incompressible flow, centrifugal force can be absorbed into the pressure gradient, producing the reduced pressure p_r:

$$\left.\frac{D\mathbf{w}}{Dt}\right|_n = -\nabla p_r + \frac{1}{Re}\nabla^2\mathbf{w} - 2\mathbf{\Omega}\times\mathbf{w} \tag{3.4}$$

where $p_r = p - \frac{1}{2}\Omega^2 r^2$. To examine the behavior of the relative flow inside the impeller passage, we investigate the reduced pressure instead of the actual pressure because the gradient of the reduced pressure affects the boundary layer behavior of the relative flow (Greitzer *et al.* 2004).

3.2.2. *Qualitative analysis of flow structures inside the impeller*

To examine flow features inside the impeller passage, we define the blade centerline coordinate s from the blade leading edge ($s = 0$) to trailing edge ($s = 1$) as shown in Fig. 3.4(a). Filleted part of the blade leading edge and blunted trailing edge are not included in the coordinate s. 100 points are equally placed from the blade leading edge to trailing edge on the blade pressure and suction surfaces. In Fig. 3.4(b), the blades are numbered from 1 to 5 in the clockwise direction, where the blade 1 is

the first blade from the volute tongue. Black dots represent monitoring points for pressure which will be discussed in section 3.3.

Figure 3.5 shows the contours of the instantaneous pressure on the impeller surface. The pressure is lowest near the hub and increases inside the impeller passage. The pressure on the blade surface is nearly uniform in the axial (x) direction (not shown). The pressure contours on the impeller surface are not circular but distorted from the pressure to suction side, meaning that at a given radial location the pressure on the blade pressure surface is larger than that on the suction surface. This is because the pressure gradient from suction to pressure side develops in a rotating passage to balance the Coriolis force. Unlike for the design condition, for the off-design condition, the pressure on the pressure surface of the blade near the volute tongue (i.e., blade 5) is much lower than those on other four blades 1 - 4 except near the trailing edge, indicating that the pressure rise along the impeller surface is impeded by the impeller-volute interaction. On the other hand, the pressure near the trailing edge of blade 5 rapidly increases owing to re-entering of high-pressure fluid from the volute at the off-design condition (section 3.3.1), which clearly deteriorates the performance of the centrifugal pump.

Figure 3.6 shows the instantaneous streamlines inside the impeller passage together with the contours of instantaneous radial velocity for the design and off-design conditions, respectively. The investigated impeller passages are one near the tongue (between blade 1-5 in Fig. 3.4(b)) and ones far from the tongue (between blade 2-3 and between blade 3-4). To identify flow separation regions near the impeller surface, only two color (red and blue) contours of the radial velocity are drawn for positive and negative values, respectively: in this way, the blue areas represent about

half of separation bubbles near the surface. For the design condition (the left column of Fig. 3.6), the blade suction and pressure sides contain small ("A" near the hub) and large ("B") separation bubbles, respectively. Streamlines and separation zones on passages away from the tongue do not notably differ from those on the passage near the tongue, indicating that for the design condition the impeller-volute interaction is weak and thus similar flow patterns are observed in all the impeller passages.

On the other hand, for the off-design condition (the right column of Fig. 3.6; lower flow rate than the designed one), another separation bubble ("C") appears on the blade suction side. Especially, along the passage near the volute tongue, much larger separation bubble ("B") is generated and persists near the end of the impeller passage due to strong impeller-volute interaction (see section 3.2.3 for further discussion). The separation bubbles, "A" and "C", remain relatively uniform in all the blade passages even at the off-design condition. These separation bubbles, especially the one on the blade pressure side ("B"), narrow the impeller passage and thus impede the pressure rise through the impeller passage. Flow separations inside the impeller passage at lower flow rates than at the designed one have been reported by previous studies (Byskov *et al.* 2003; Pedersen *et al.* 2003; Posa *et al.* 2015, 2016).

We investigate instantaneous blade-to-blade velocity distribution at constant radius $r/R_2 = 0.75$ between the blade 1-5, 2-3, and 3-4 in Fig. 3.7. Radial velocity distribution is higher near the blade suction side because of the potential flow effect of the relative eddy explained earlier. This higher radial velocity distribution along the blade suction surface contributes to strong vortical structures inside the impeller. Low and even negative radial velocity region is shown indicating large recirculation zone

on the blade pressure side. For the design flow rate, blade-to-blade radial velocity exhibits relatively uniform distribution in all impeller passages even near the tongue. On the other hand, for the off-design flow rate, negative radial velocity region becomes larger near the tongue than those in other passages. This clearly shows that strong blade-tongue interaction induces highly unsteady flow features even inside the impeller passage for the off-design condition.

3.2.3. *Quantitative analysis of flow characteristics inside the impeller*

To investigate the behavior of the relative flow inside the impeller passage, we compute coefficients of the reduced pressure and skin-friction along the blade centerline coordinate s. They are defined by the following equations:

$$C_{p_r} = \frac{\langle p \rangle - 0.5\rho\Omega^2 r^2 - p_\infty}{0.5\rho U_2^2}, C_f = \frac{\tau_w}{0.5\rho U_2^2} \tag{3.5}$$

where $\tau_w = \mu\partial \langle w_s \rangle / \partial n$. τ_w and w_s are wall shear stress along the blade centerline and velocity in the coordinate s. Reference pressure p_∞ is defined at the center of the duct inlet. $\langle \cdot \rangle$ indicates the phase averaging operator. The phase averaging is performed as

$$\langle f(\mathbf{x}, t) \rangle = \frac{1}{N} \sum_{n=0}^{N-1} f(\mathbf{x}, t + \frac{2\pi n}{N_b \Omega}), \tag{3.6}$$

where 500 instantaneous flow fields on LES3 are phase-averaged for the present study (corresponding to 100 impeller revolutions).

Figure 3.8 exhibits coefficients of the reduced pressure and skin-friction along the blade centerline. As flow rates increase, a stronger pressure gradient is created between the pressure and suction side of a blade to balance the increased Coriolis force. Thus, the pressure difference between the blade pressure and suction surfaces is larger for the design flow rate

than that for the off-design flow rate ($\phi_{\text{off}} = 0.57\phi_{\text{d}}$ in the present study). As a result, the larger torque is required as more fluid is pumped.

At the design condition along the blade pressure side (solid lines of Fig. 3.8(a)), fluid experiences adverse pressure gradient after passing the blade leading edge. The corresponding skin-friction coefficient indicates that flow is decelerated and eventually separates due to the adverse pressure gradient. Note that the actual pressure keeps increasing along the blade centerline because of the centrifugal acceleration in contrast to the reduced pressure. The adverse pressure gradient decreases, and flow reattaches forming a large recirculated region, ("B" in Fig. 3.6). At the trailing edge, pressure difference between the pressure and suction side is decreased and the Coriolis force drives the relative flow in the direction opposite to the impeller rotation. This results in curvature of the relative streamline and low pressure at the trailing edge of the blade pressure side generating steep favorable pressure gradient. Because of the favorable pressure gradient near the trailing edge, fluid is accelerated with increasing skin-friction coefficient.

Along the blade suction side (dash-dotted lines of Fig. 3.8(a)), small area of steep adverse pressure gradient is located creating a small recirculation zone ("A" in Fig. 3.6) after the leading edge of the blade. Following the adverse pressure gradient, relatively moderate favorable pressure gradient is observed up to nearly the trailing edge. This results in well-attached flow and moderate variation of the skin-friction along the blade suction surface. Note that coefficients of the blade pressure and suction side do not meet at the leading and trailing edge because the filleted leading edge and blunted trailing edge are not included in the centerline coordinate s. For the design condition, similar characteristics

between five blades are found except for the pressure along the blade pressure side. Due to the blade-tongue interaction, the larger pressure gradient along the blade pressure side is observed near the tongue (i.e., blade 5) than the others.

For the off-design condition, wall flow characteristics shows similar aspects with that for the design condition. The strong adverse pressure gradient along the blade pressure surface induces large recirculated area. Steep favorable pressure gradient with increasing skin friction is observed near the blade trailing edge. Along the blade suction surface, small region of adverse pressure gradient and flow separation are also generated near the blade leading edge. Smaller pressure gradient and skin friction for the off-design condition than those for the design condition are observed indicating the effect of the lower mean flow rate for the former condition. Due to the strong blade-tongue interaction for the off-design condition, the pressure on the blade pressure side near the tongue (i.e., blade 5) is much lower than those on other four blades except near the trailing edge. On the other hand, the pressure near the trailing edge of blade 5 rapidly increases owing to re-entering of high-pressure volute flow through the radial gap between the impeller and the tongue, delaying the reattachment of the separation bubble (section 3.3.1). This produces highly unsteady separation bubbles on the blade pressure side for the off-design condition.

3.3. Impeller-volute interaction

3.3.1. *Trailing vortices shed from blades and flow separation at the tongue*

The contours of the instantaneous vorticity magnitude at the volute mid-span on window W2 are shown in Fig. 3.9 for the design and off-design conditions. For the design condition, trailing vortices are shed

from the rotating blade, and the vortices near the blade suction surface advect downstream and interact with the trailing vortices in the volute. But these vortices do not interact with those from the following blade. At the off-design condition, the vortices from the blade suction surface are much weaker than those observed for the design condition due to the lower mean flow rate. Nonetheless, the vortices shed from the blade trailing edge are quite strong, convect more in the azimuthal direction than those of the design condition, and interact with the ones from the next blade, creating a wider distribution of strong vortices in the volute. These vorticity distributions in the volute were also observed by previous experiments (Paone *et al.* 1989; Dong *et al.* 1992; Chu *et al.* 1995; Dong *et al.* 1997). Especially, Paone *et al.* (1989) reported that vortices become stronger and more widely distributed with decreasing flow rate, which is well represented in the present study.

Fig. 3.10 shows the contours of the instantaneous vorticity magnitudes at the volute mid-span near the volute tongue. At the design condition, trailing vortices shed from rotating blades and near-wall vortices along the blade suction side are observed. Vorticity distribution near the tongue is modest indicating the weak interaction between the flow and the tongue. At the off-design condition, strong vortices in broader areas are found in the volute. Also, vortices near the tongue interact with boundary layer flows of the blade pressure side. The strong blade-tongue interaction induces high levels of vorticity magnitude and highly turbulent flow near the toungue.

Fig. 3.11 shows the time evolutions of the instantaneous vorticity magnitude and streamlines near the volute tongue for the design and off-design conditions. At the design condition, the vortices shed from the blade trail-

ing edge start to interact with the volute tongue when they pass (Zhang *et al.* 2016), but the interaction is weak and thus causes relatively weak vortices near and downstream of the volute tongue. At the off-design condition, the interaction is very strong, producing strong vortices near and downstream of the volute tongue. This difference between two operating conditions is caused by the flow entering into the gap between the volute tongue and impeller from the volute. That is, for the case of design condition, most flow from the volute exits to the discharge pipe (although there is a small separation bubble on the outer surface of the volute tongue), whereas a large amount of volute flow enters into the gap (as mentioned above) and the flow even separates on the volute upstream side at the off-design condition. According to Barrio *et al.* (2010) and Zhang *et al.* (2016), the discharged fluid from the volute flows smoothly along the volute tongue without flow separation at the design condition, but, at higher flow rates, the flow separation occurs and separated flow moves toward the discharge pipe. The present LES shows that with the present pump configuration flow separation at the volute tongue still occurs even at the design condition and separated flow moves toward the discharge pipe. This result suggests that a flow rate slightly lower than the designed one may have no separation at the present volute tongue.

3.3.2. *Pressure fluctuations along the impeller periphery*

Pressure fluctuations, which are primary causes of noise and vibration of a pump, are widely investigated via experiments (González *et al.* 2002; Chu *et al.* 1995; Barrio *et al.* 2011; Gao *et al.* 2017), URANS (Majidi 2005; González *et al.* 2002; Shi 2001; Barrio *et al.* 2011), and LES (Zhang *et al.* 2019; Posa & Lippolis 2019; Posa 2021). Although there have been

extensive studies on pressure fluctuations inside centrifugal pumps, investigation on pressure fluctuations using the triple decomposition (Hussain & Reynolds 1970; Reynolds & Hussain 1972) has been rarely done. Therefore, we perform the triple decomposition of the instantaneous pressure as follows:

$$p(\mathbf{x}, t) = \bar{p}(\mathbf{x}) + \hat{p}(\mathbf{x}, t) + p'(\mathbf{x}, t) \tag{3.7}$$

where $\bar{p}, \hat{p}, p'$ are the time-averaged, time-periodic, and turbulent fluctuating components, respectively. Then, the periodic component is computed by:

$$\hat{p} = \langle p \rangle - \bar{p} \tag{3.8}$$

where the phase average is defined by the equation 3.6. To investigate pressure fluctuations, we measure instantaneous pressure at constant $r/R_2 = 1.03$ on the volute mid-span as seen in Fig. 3.4(b). The pressure signal is collected during 100 revolutions on LES3 grids. In the present study, we obtain a fluctuating pressure p which is filtered in space. As noted by previous studies Hussain & Reynolds (1970); Reynolds & Hussain (1972), fluctuating components of the periodic motion and turbulence are uncorrelated, thus following is satisfied:

$$\overline{\hat{p}^2} + \overline{p'^2} = \overline{(\hat{p} + p')^2} = \overline{(p - \bar{p})^2} \tag{3.9}$$

Fig. 3.12 shows the distributions of the rms pressure fluctuations, $\hat{p}$, p', and $\hat{p}+p'$ at $r/R_2 = 1.03$ along the azimuthal direction. For the design condition, p'_{rms} is much smaller than $\hat{p}_{rms}$, but becomes large near the tongue ($\xi = 0°$). On the other hand, $\hat{p}_{rms}$ shows the modulated azimuthal distribuition with five (i.e., the number of the blades) local maxima and minima, agreeing with previous studies (Barrio *et al.* 2010; González *et al.*

2002; Parrondo *et al.* 2002). Especially, Parrondo *et al.* (2002) stated that two major sources of pressure fluctuations along the impeller periphery are pertubations induced by continuous blade rotation and wave propagation caused by the interaction between the flow and the tongue. At peaks, the mutual effect of these two sources become strong, generating strong pressure fluctuations. The triple decomposition clearly shows this modulated pattern of pressure fluctuations originate from periodic fluctuations. For the design condition, p'_{rms} is smaller than $\hat{p}_{rms}$ even near the tongue. Hence, total fluctuations are mainly determined by $\hat{p}$. For the off-design condition, p'_{rms} increases rapidly near the tongue and is dominant there, and $\hat{p}_{rms}$ is larger than p'_{rms} elsewhere. $\hat{p}_{rms}$ shows the modulated azimuthal distribuition with larger peak-to-peak difference indicating stronger impeller-volute interaction for the off-design condition. Total fluctuations are mainly determined by the turbulence near the tongue and by both fluctuations elsewhere.

3.3.3. *Leakage through the radial gaps*

Many centrifugal pumps have cavities between the impeller and volute casing for structural stability and cost reduction, and thus suffer from leakage through radial gaps (Fig. 2.1(a)) into these cavities (Gülich 2008). However, due to high Reynolds number flow and complicated shapes of centrifugal pumps, studies on this leakage have been limited. To understand the characteristics of this leakage, we first investigate the cross-plane flow inside the volute.

Fig. 3.13 shows the instantaneous cross flows on four different cross-flow (x-r) planes for the design and off-design conditions. The cross-plane flow inside the volute is much stronger for the off-design condition than

that for the design condition. For the off-design condition, right after the volute tongue (on F1 plane) at the current blade positions, the flow from the impeller impacts on the volute casing and generates strong clockwise (viewed from upstream-to-downstream direction) vortex inside the volute, inducing a strong reverse flow from the bottom cavity to the volute (i.e. reverse leakage). This secondary vortex grows in size as the flow moves downstream (F2 and F3 planes). On F3 plane, the center of the secondary vortex moves towards the radial gap between the impeller and volute casing, and thus the reverse leakage is blocked by this secondary vortex. Complex interactions between the flows from the impeller and volute are observed in between the upper and lower radial gaps. On F4 plane (which locates 5°ahead of the volute tongue), strong leakage flows occur on both gaps mainly due to strong pressure gradient formed in this region, as discussed in the below. This secondary vortex is also observed for the design condition but its development is much slower than that for the off-design condition.

Figs. 3.14(a) and (b) show the contours of the instantaneous pressure and axial velocity on F4 plane, respectively. At the design condition, the pressure increases slowly in the radial direction from impeller passage to the volute casing, and the pressure field is more or less homogeneous in the axial direction. Therefore, the leakages to top and bottom cavities are low. However, at the off-design condition, the pressure rapidly increases in the radial direction and the volute pressure is much higher than that at the design condition, resulting in also high pressure gradient in the axial direction at the radial gaps. The leakages to the cavities, therefore, are quite large and create a significant loss in the pump performance.

Fig. 3.15 shows the contours of the time-averaged pressure on the

volute mid-span for the design and off-design conditions. At the design condition, the pressure rise in the volute is relatively mild. On the other hand, at the off-design condition, the pressure normalized by the blade-tip rotating velocity rapidly increases along the volute passage, and a considerable amount of leakage occurs especially upstream of the volute tongue due to high pressure inside the volute exit area. To quantitatively analyze the leakage, the azimuthal distribution of leakage is computed as

$$u_{x,leak}(\theta) = \frac{1}{A} \int_{\theta-\frac{1}{2}\Delta\theta}^{\theta+\frac{1}{2}\Delta\theta} \int_{R_i}^{R_o} \bar{u}_x \; r dr d\theta \tag{3.10}$$

where R_i and R_o are the radial distances to the impeller and volute casing, respectively (see Fig. 3.14(a)), A is the integration area, and $\bar{u}_x$ is the time-averaged axial velocity at the radial gap.

Fig. 3.16 shows the distributions of the leakage flow on the upper and lower radial gaps in the azimuthal direction for the design and off-design conditions. Note that the leakages on the upper and lower radial gaps to the cavities correspond to positive and negative axial velocities, respectively. As shown, the leakage is strongest near the volute tongue, and the flow from the cavities to the volute area (i.e. reverse leakage) also exists, especially downstream of the volute tongue, because of the continuity (see also Fig. 3.13). At the off-design condition, most of the leakage is formed near the volute tongue, and the leakage is very strong such that its magnitude is up to 20% of blade-tip rotating velocity. The amount of leakages through the upper and lower radial gaps is about 27% of the flow rate ϕ_{d} for the design condition, whereas, for the off-design condition, the leakages to the cavities are quite large, amount to 67% of ϕ_{off}. These leakages come back to the volute area because of the continuity; see the areas of reverse leakage (positive and negative axial

velocities on the lower and upper radial gaps, respectively) in Fig. 3.16.

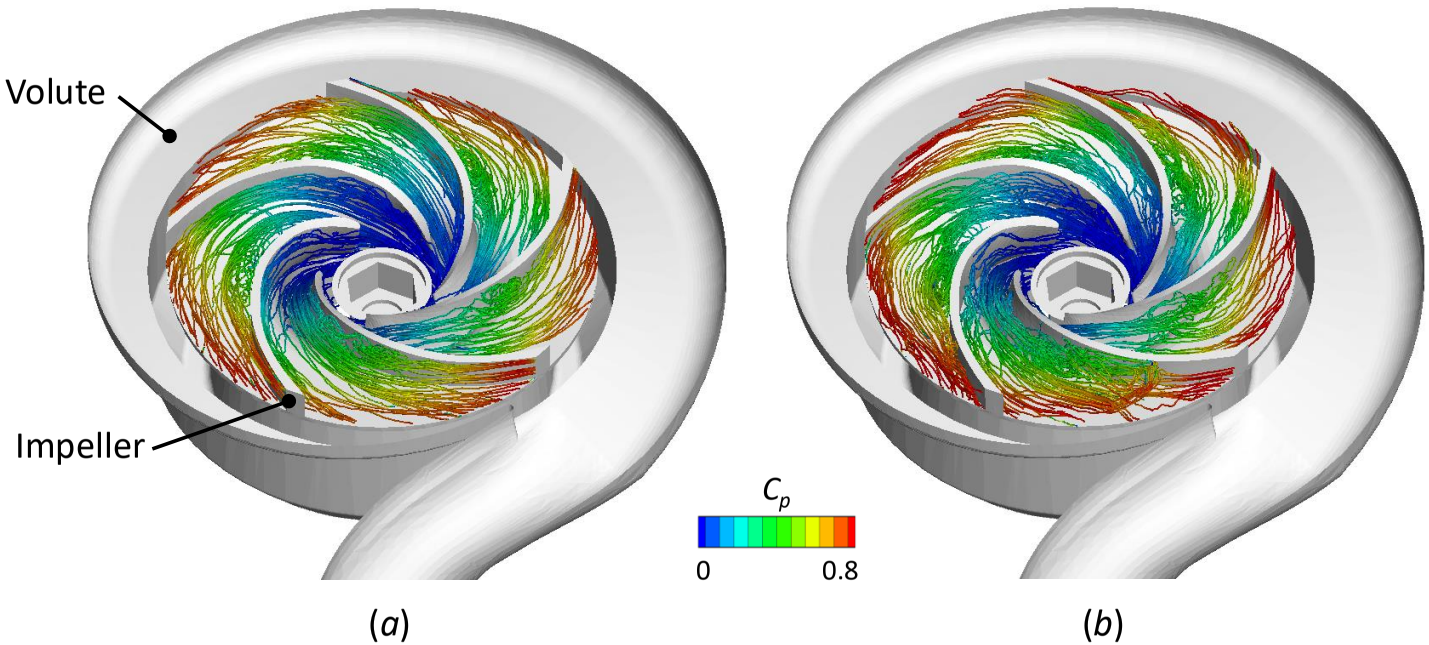

Figure 3.1: The instantaneous streamlines together with the pressure coefficient inside the impeller passage : (a) design condition; (b) off-design condition

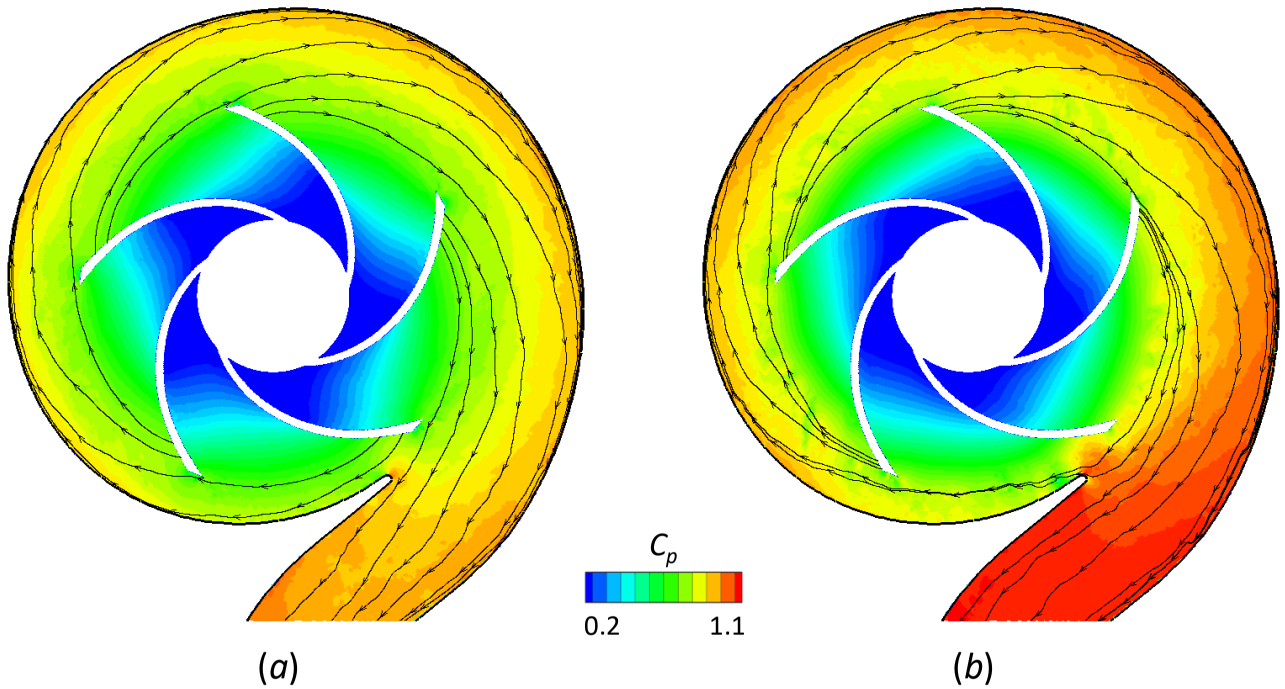

Figure 3.2: The instantaneous streamlines together with contours of the pressure at the volute mid-span : (a) design condition; (b) off-design condition

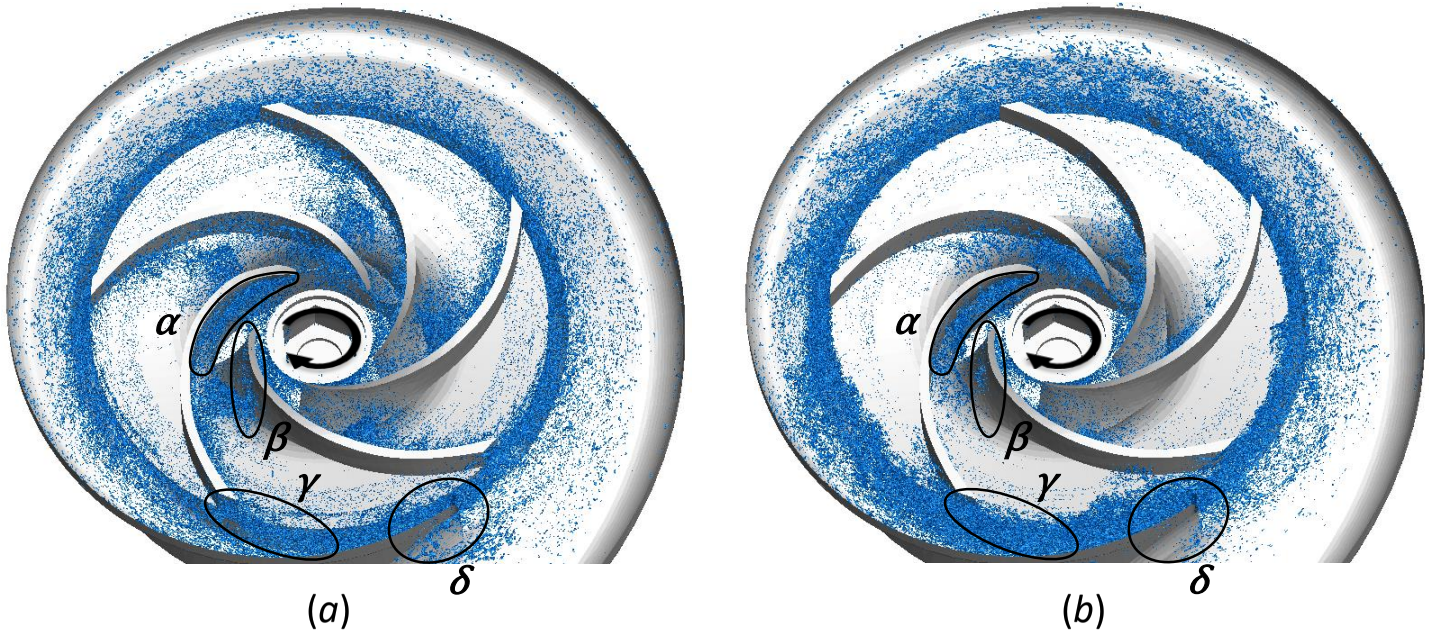

Figure 3.3: Instantaneous vortical structures, identified by the iso-surfaces of $\lambda_2 = -180$ (Jeong & Hussain 1995) : (a) design condition; (b) off-design condition

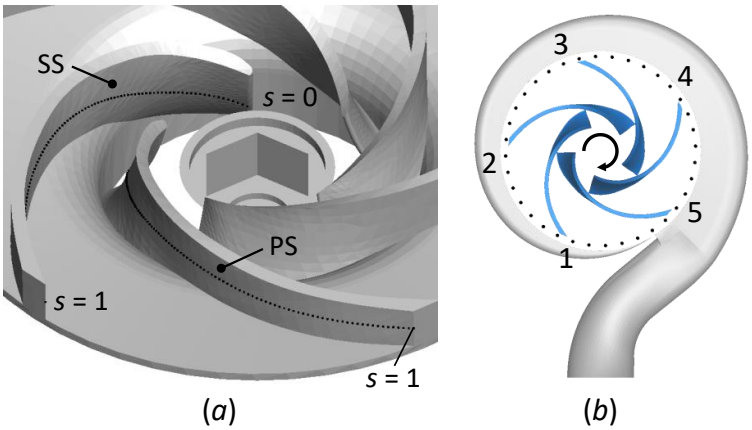

Figure 3.4: Blade centerline coordinate s and impeller blades 1-5 for the blade position angle of $\varphi = 54°$. In (a), PS and SS represent the blade pressure and suction surfaces, respectively. In (b), 36 black dots denote monitoring positions at $r/R_2 = 1.03$.

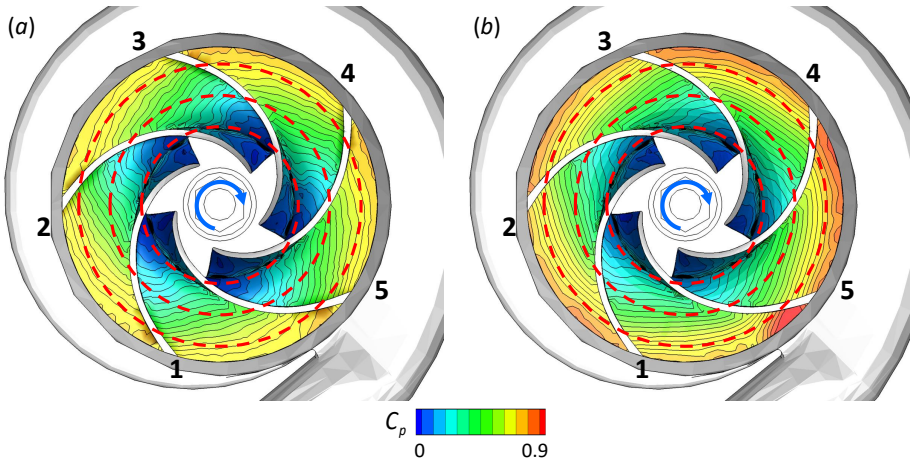

Figure 3.5: Contours of the instantaneous pressure on the impeller surface (plan view) : (a) design condition; (b) off-design condition. Here, red dashed curves correspond to the circles with the radii of 0.5, 0.7 and $0.9R_2$.

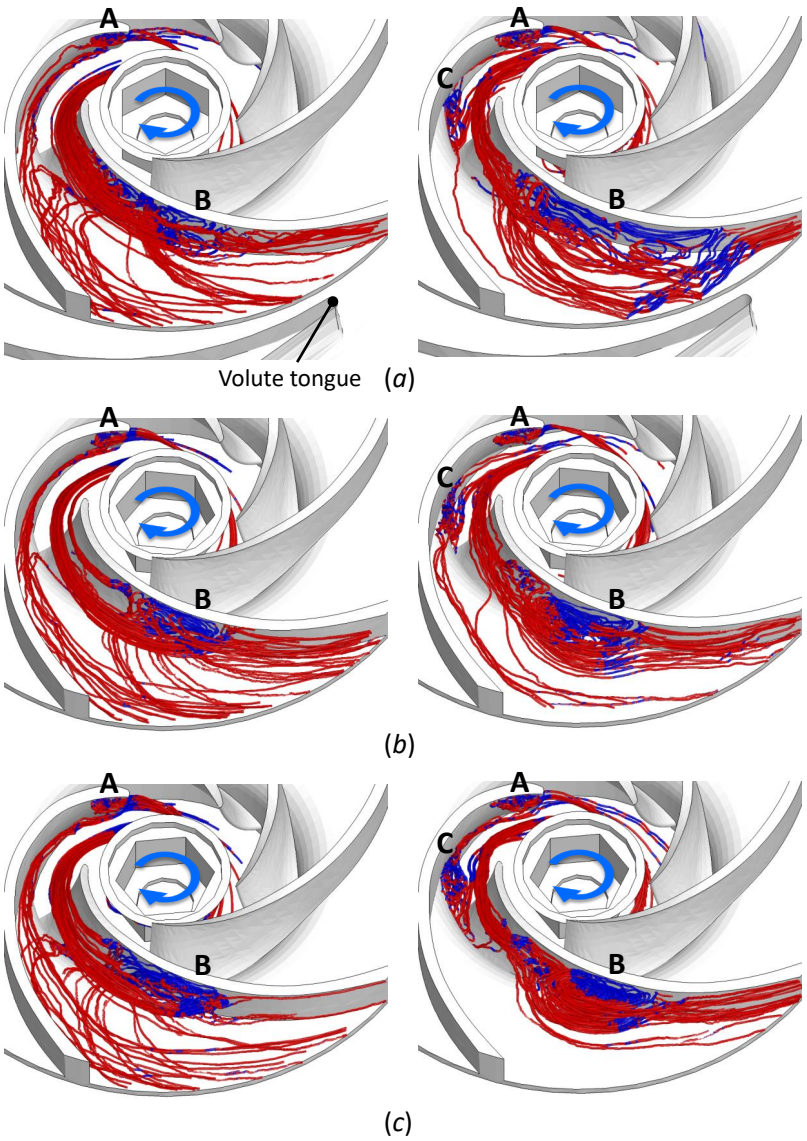

Figure 3.6: Instantaneous streamlines for the design (left) and off-design (right) conditions: (a) between blade 5-1; (b) between blade 2-3; (c) between blade 3-4 (Fig. 3.4(b)). Here, red and blue colors on the streamlines denote positive and negative instantaneous radial velocities, respectively.

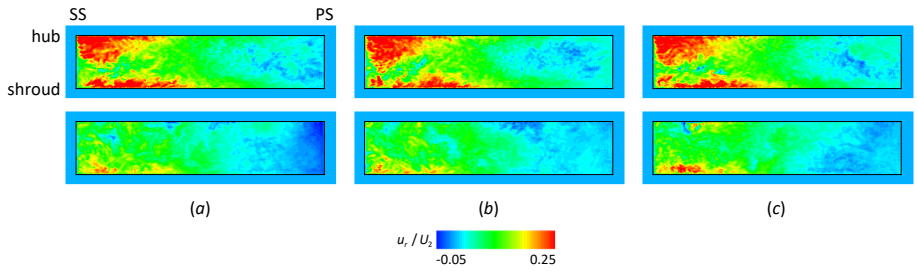

Figure 3.7: Contours of the instantaneous radial velocity at $r/R_2 = 0.75$ for the design (top) and off-design (bottom) conditions: (a) between blade 5-1; (b) between blade 2-3; (c) between blade 3-4 (Fig. 3.4(b))

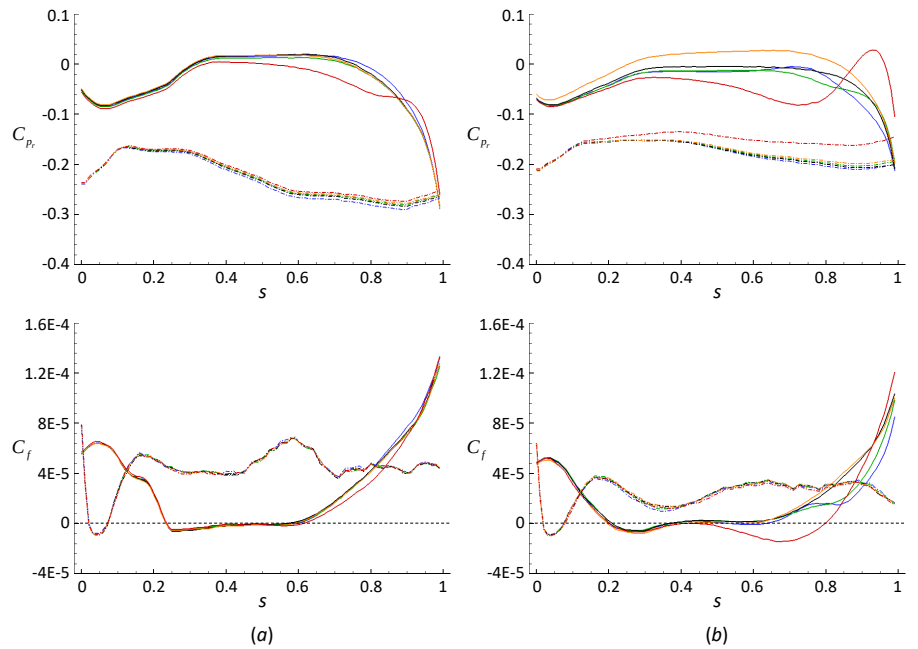

Figure 3.8: Reduced pressure (top) and skin-friction (bottom) coefficients ($\varphi = 54°$): (a) design condition; (b) off-design condition. ——— along the pressure side; - · - · -, along the suction side; ———, blade 1; ———, blade 2; ———, blade 3; ———, blade 4; ———, blade 5.

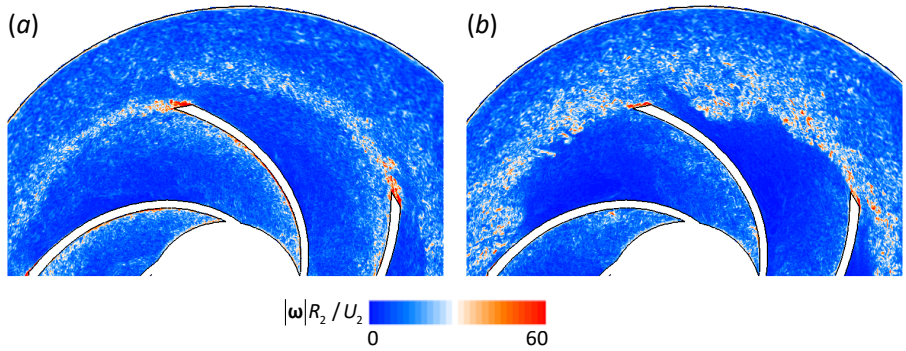

Figure 3.9: Contours of the instantaneous vorticity magnitude at the volute mid-span on window W2 (Fig. 2.1(b)): (a) design condition; (b) off-design condition

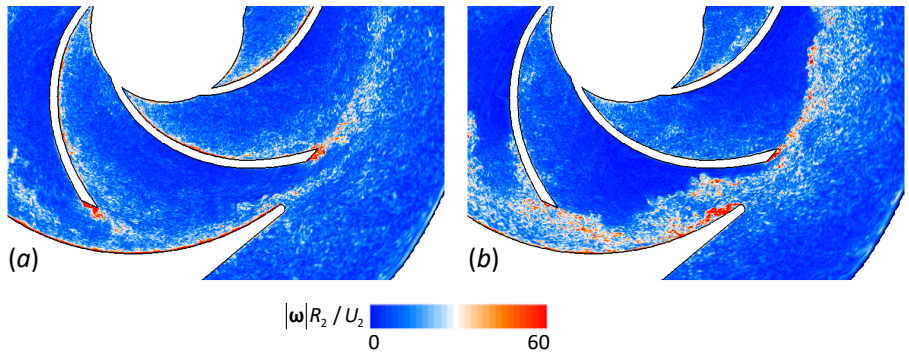

Figure 3.10: Contours of the instantaneous vorticity magnitude at the volute mid-span on window W1 (Fig. 2.1(b)): (a) design condition; (b) off-design condition

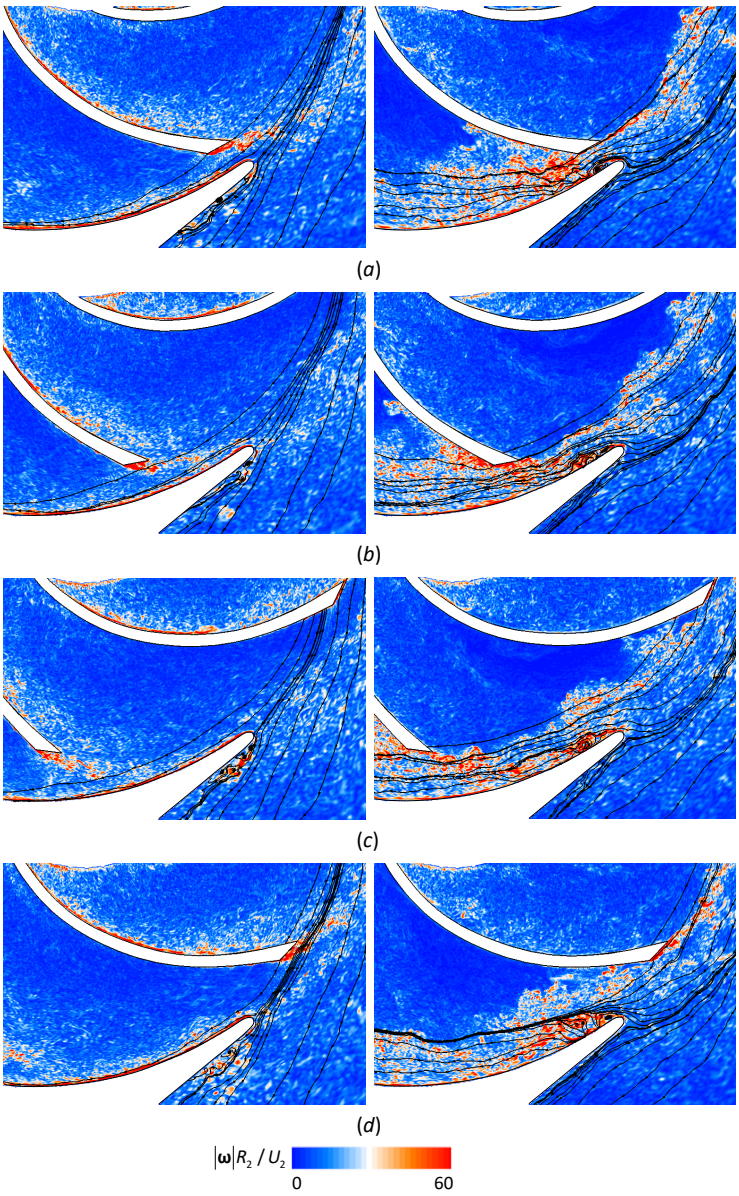

Figure 3.11: Time evolutions of the instantaneous vorticity magnitude and streamlines near the tongue at the volute mid-span for the design (left) and off-design (right) conditions: (a) $\varphi = 0°$; (b) $\varphi = 18°$; (c) $\varphi = 36°$; (d) $\varphi = 54°$

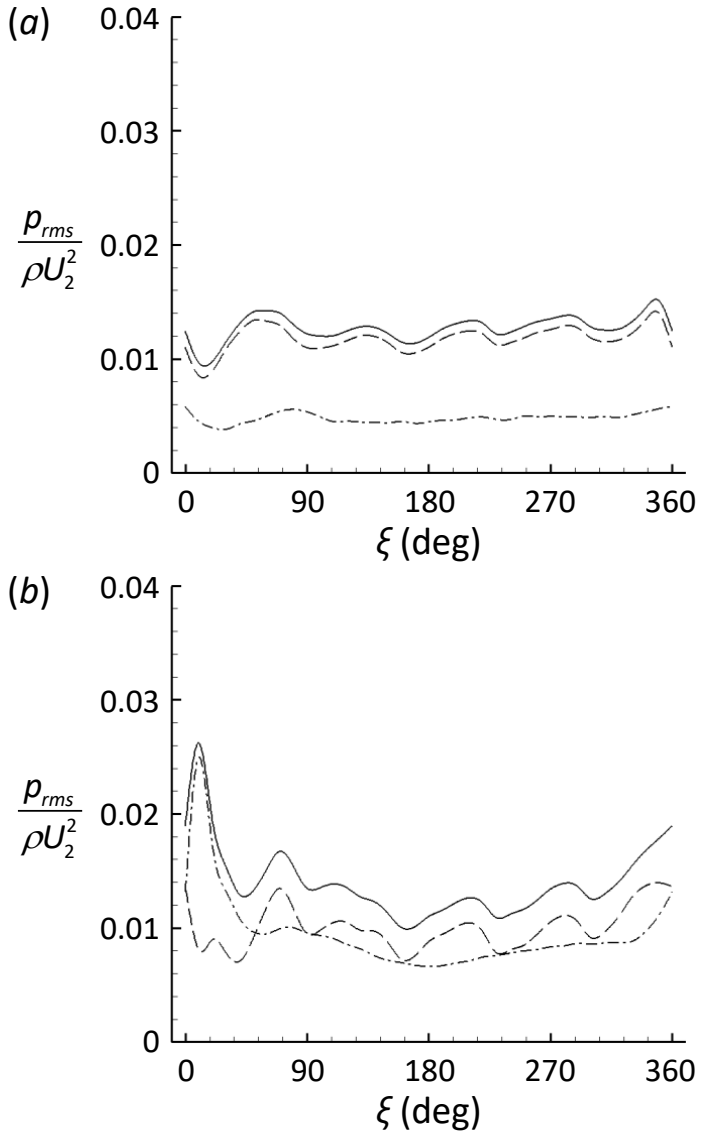

Figure 3.12: Distributions of the rms pressure fluctuations at $r/R_2 = 1.03$ on the volute mid-span: (a) design condition; (b) off-design condition. - - - -, $\hat{p}$; - · - · -, p'; ——— $\hat{p} + p'$.

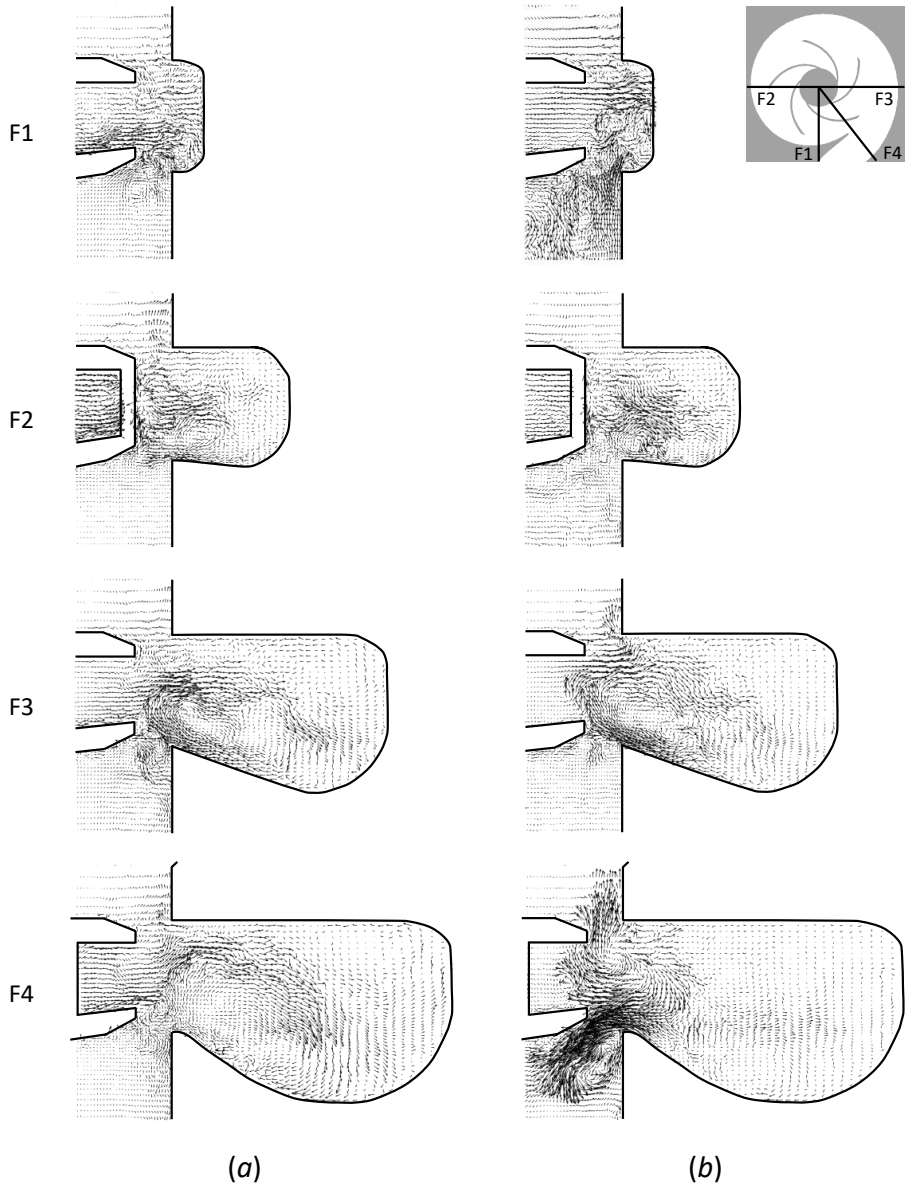

Figure 3.13: Instantaneous cross-flow vectors on cross-flow planes, F1 - F4, inside the impeller-volute passage: (a) design condition; (b) off-design condition

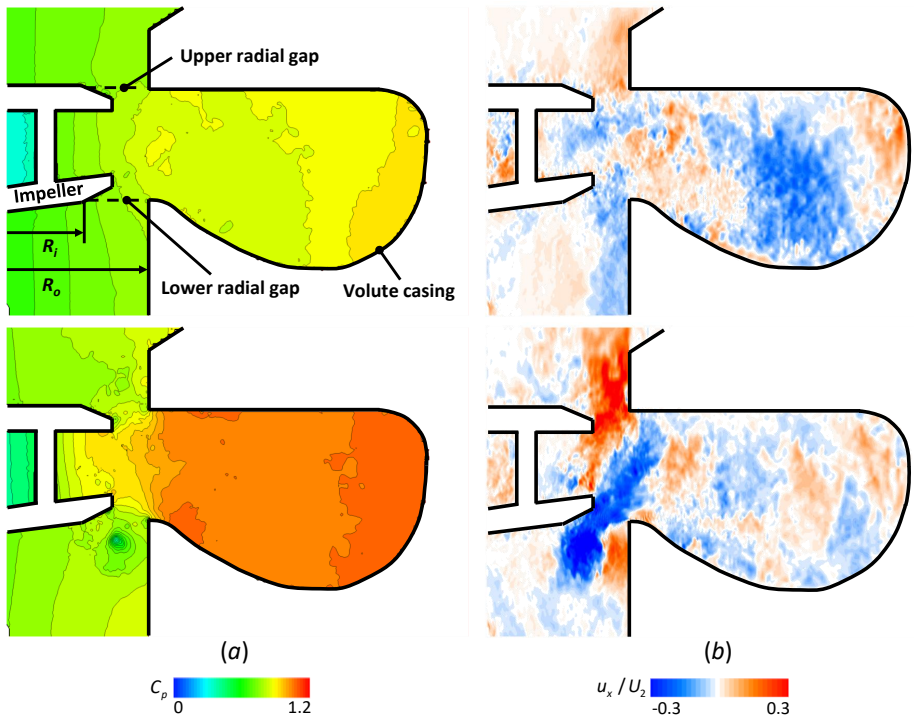

Figure 3.14: Instantaneous leakage flows on plane F4 (Fig. 3.13) at the design (top) and off-design (bottom) conditions: (a) pressure; (b) axial velocity

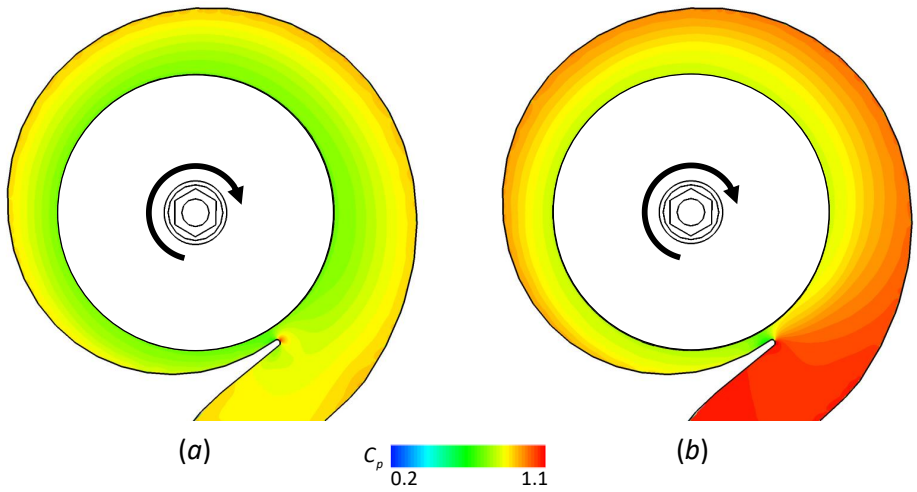

Figure 3.15: Contours of the time-averaged pressure at the volute mid-span: (a) design condition; (b) off-design condition

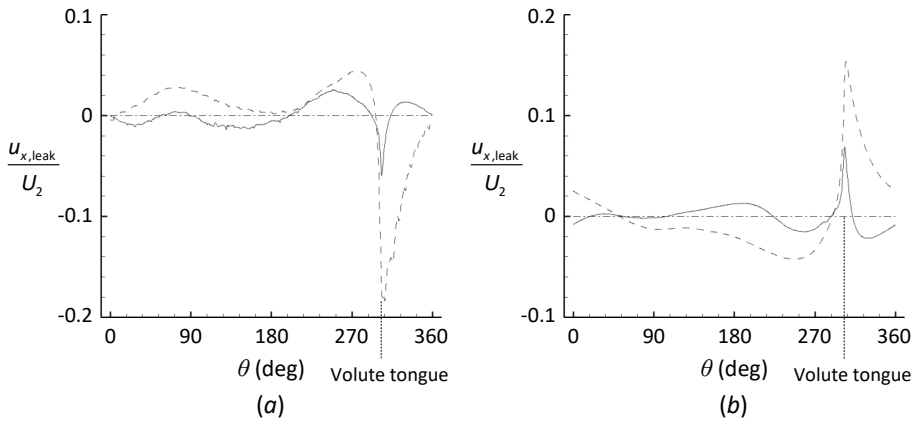

Figure 3.16: Azimuthal distributions of the time-averaged leakage through radial gaps: (a) lower radial gap; (b) upper radial gap. ——— design condition; - - - -, off-design condition.

Chapter 4

Summary and concluding remarks

In the present study, we performed LES with an immersed boundary method in a non-inertial reference frame (Kim & Choi 2006) to investigate the flow charactristics in a volute-type centrifugal pump operating at the design and off-design conditions at $Re = 1,740,000$. Both the impeller and volute casing were considered. Separation bubbles were observed inside impeller passages at both flow conditions, but larger separation bubbles, especially near the blade pressure side, formed at the off-design condition in addition to a new separation bubble on the blade suction side. Reduced pressure and skin friction along the blade centerline were investigated to the behavior of the relative flow inside the impeller passage. Adverse pressure gradient was observed along the pressure and suction side of the blade generating separation bubbles.

Strong blade-blade and impeller-volute interactions occurred at the off-design condition. Vortices were shed from the blade trailing edge both at the design and off-design conditions. However, at the off-design condition, these vortices interacted with those from the following blade, causing

broader areas of stronger vortices inside the volute. At the design condition, most flow from the volute passage exited to the discharge pipe and only a small section went back to the volute. Therefore, the impeller-volute interaction was relatively weak. However, at the off-design condition, a large amount of flow went back to the volute and flow separation occurred at the volute upstream, creating high vorticity region near the tongue and strong interaction with the vortices shed from the blade trailing edge.

Triple decomposition of the pressure fluctuation along the impeller periphery was performed. For the design condition, turbulent fluctuations increased near the tongue but were still smaller than periodic fluctuations. Periodic fluctuations exhibited the modulated distribution in azimuthal direction contributed by continuous blade rotation and blade-tongue interaction. On the other hand, for the off-design condition, turbulent fluctuations increased rapidly near the tongue becoming much larger than those by periodic components. Thus, total fluctuations were mainly determined by the turbulence near the tongue due to the strong impeller-volute interaction.

Leakage flow to the cavities existing between the impeller and volute is another flow loss. At the design condition, the pressure rise from the impeller to volute was relatively small and the pressure was homogeneous in the axial direction, resulting in small leakage to the cavities. However, at the off-design condition, the pressure rise from the impeller to volute was quite large and thus a large pressure gradient existed in the axial direction, producing large leakage to the cavities. At the off-design condition, most leakage occurred near the volute tongue due to strong impeller-volute interaction. On the other hand, azimuthal vortices were

observed inside the volute at both flow conditions, and they grew along the volute passage. A secondary motion caused by these vortices also significantly affected the leakage to the cavities, especially for the off-design condition.

In the present study, we identified various flow losses in the volute-type centrifugal pump at the off-design condition, such as large separation bubble on the blade pressure side, secondary motion inside the volute, separation at the volute tongue, leakage to top and bottom cavities existing between the impeller and volute, leakage of fluid near the volute exit returning to the gap between the volute tongue and impeller, and interaction of blade wakes. Most of these losses are caused by the impeller-volute interaction with larger losses for the off-design condition due to the strong impeller-volute interaction.

Part II.

LES vs. URANS: turbulent flow in a centrifugal pump

Chapter 1

Introduction

Centrifugal pumps, which are the most common type of pumps, are widely employed for various industrial applications and consume a lot of electricity worldwide. According to the European Commission (Reeves 2001), 14% of the total electricity in industry and commerce of the EU is spent by pumps, of which centrifugal pumps account for around 73%. Also, World Pumps (2020) reported that more than 300 TWh of electricity, out of about 3,300 TWh of total European electricity consumption per year, is used by electric pumps. The energy consumption corresponds to the output of 30 large coal-fired power plants. With growing interest in energy saving, understanding the flow characteristics and losses inside pumps is getting more and more important.

Although centrifugal pumps have been utilized and studied for long time, an accurate prediction of the flow is still difficult due to complex three-dimensional flow phenomena caused by high speed rotation of the rotor and rotor-stator interaction. Examples of those flow phenomena include flow separation, pressure fluctuations, secondary flow, back-flow,

and interaction of blade wakes.

To predict the unsteady flow characteristics inside pumps, simulation with unsteady Reynolds-averaged Navier-Stokes equations (URANS) has been widely used. Barrio *et al.* (2010) investigated pressure pulsations associated with the impeller-volute interaction at various flow rates in a volute-type centrifugal pump. The largest pressure pulsations occurred near the volute tongue because of the strong blade-tongue interaction. Although agreement between numerical and experimental data was good around the design flow rate, significant differences were observed at off-design conditions.

Feng *et al.* (2009*a*) studied turbulent flows in a centrifugal pump with diffuser vanes for the design flow rate by URANS, particle image velocimetry (PIV), and laser Dopper velocimetry (LDV). They observed the jet-wake flow pattern near the impeller outlet where high relative velocity with low turbulence region on the pressure side and low relative velocity with high turbulence region on the suction side were developed. Although their numerical results predicted the pump head accurately and captured the overall trend of the relative velocity and turbulence intensity inside the pump, quantitative comparison revealed considerable discrepancy between simulation and experiments exists especially for the turbulence intensity.

Yan *et al.* (2017) added splitter blades to the impeller and changed the double volute of trapezoidal cross section to single volute of circular cross section with an increased radial gap between impeller and volute tongue. They simulated flow in redesigned pump reporting improved efficiency and reduced pressure pulsations. In addition to these studies, URANS has been used to study the impeller-volute interaction (González *et al.* 2002;

Asuaje *et al.* 2005; Cheah *et al.* 2011; Tan *et al.* 2015), impeller-diffuser interaction (Shi 2001; Stel *et al.* 2013), unsteady impeller force (González *et al.* 2006; Barrio *et al.* 2011), and to enhance the pump performance by modifying pump geometry (Barrio *et al.* 2008; Spence & Amaral-Teixeira 2009).

However, as noted by previous studies (Iaccarino *et al.* 2003; Strelets 2001; Shimada & Ishihara 2002), URANS performs well for flows where periodic fluctuations are dominant but worse for highly turbulent flows. Decreased performances of URANS for turbulent pump flows at off-design conditions are also reported by previous studies (Barrio *et al.* 2008, 2010; Feng *et al.* 2009*a*; González *et al.* 2002, 2006). Therefore, with recent advances in computing power, large eddy simulation (LES) has been adopted to accurately simulate turbulent flows inside pumps for off-design conditions as well as for the design condition.

Kato *et al.* (2003) simulated the flow in a mixed-flow pump at various flow rates using the standard Smagorinsky model with Van Driest damping function. The predicted pump head by LES showed good agreement with experiments but the stall point was predicted at a somewhat lower flow rate than experiments. The phase-aveaged distributions of the meridional and tangential velocity by LES were in good agreement with those measured by a two-dimensional LDV.

Byskov *et al.* (2003) conducted both LES and steady RANS of flows in a six-bladed centrifugal pump impeller at design and off-design conditions, and compared the results with PIV data. The radial and tangential velocity profiles in the impeller mid-height by LES exhibited satisfactory agreement with PIV, whereas those by RANS showed substantial disagreement. Especially for the off-design condition, RANS did not re-

produce the stall phenomena which was resolved in LES.

Posa *et al.* (2011) conducted LES using the standard Smagorinsky model (Smagorinsky 1963) and the filtered structure function model (Ducros *et al.* 1996) in a centrifugal pump with diffuser vanes. They compared the numerical resutls with PIV data (Boccazzi *et al.* 2009). The phase-averaged velocity distribution at the diffuser mid-span by the latter model was in good agreement with experimental data, whereas that by the former model failed predicting flow separation accurately resulting in considerable velocity mismatch near the wall. The increased turbulent kinetic energy and flow separation inside the impeller and diffuser at the off-design condition were also studied by LES (Posa *et al.* 2015, 2016) with the wall-adapting local eddy-viscosity model (Nicoud & Ducros 1999). Posa & Lippolis (2018, 2019) rotated the diffuser vanes around their mid camber to study the effect of the diffuser incidence angle and the impeller-diffuser gap on turbulent flows like flow separation, turbulent kinetic energy, and pressure fluctuations. With the modified diffuser geometry, the pump efficiency was improved with decreased flow separation, turbulent kinetic energy, and pressure fluctuations for the off-design condition. However, the modification resulted in lower performance at the design condition. More recently, Posa (2021) rotated the diffuser vanes around their leading edge to separate the effect of the diffuser incidence angle from the impeller-diffuser gap. Their results revealed, at the off-design condition, the lower incidence angle over the diffuser vanes is the main source of higher pressure rise, whereas the larger impeller-diffuser gap is the main source of the reduced pressure fluctuations.

In our previous study (Kye *et al.* 2018), LES was conducted to study turbulent flows in a volute-type centrifugal pump at design and off-design

conditions. Pressure rise predicted by LES showed very good agreement with experiments even for the off-design condition. Unsteady flow losses such as flow separation, secondary flows, vortices shed from the blade trailing edge, and leakages to cavities were investigated. Most of these losses were increased at the off-design condition due to the strong impeller-volute interaction.

These previous studies have shown LES can be a better alternative to URANS which predicts the flow well at the design condition but does not at off-design conditions (Byskov *et al.* 2003; Lucius & Brenner 2010; Posa *et al.* 2011). However, a systematic comparison to investigate whether LES is necessary to predict turbulent flows in pump has been very limited. As mentioned above, Byskov *et al.* (2003) compared LES results in a centrifugal impeller to steady RANS solutions, and showed that LES accurately predicted unsteady stall at the off-design condition better than RANS did. However, their studies neglected the stationary volute casing, and thus did not include the impeller-volute interaction.

For the design flow condition, Torner *et al.* (2017) simulated flow in an implantable axial pump utilized as a ventricular assist device using LES and URANS. They revealed that LES and URANS exhibited analogous results for integral quantities and mean velocity fields, but showed substantial discrepancy in the turbulent kinetic energy.

Nagahara *et al.* (2005) investigated the flow in a four-stage centrifugal pump with diffuser vanes at the design condition using LES and URANS. The computed pump head, velocity distribution at the impeller inlet and diffuser outlet by LES and URANS demonstrated reasonable agreement with experiments. However, URANS did not capture vortices in the diffuser passage which were observed by LES.

In spite of these studies, the prediction capabilities by LES and URANS for the flow in a centrifugal pump have not been thoroughly investigated, especially at the off-design condition. In the present study, we conduct both LES and URANS for flow in a volute pump for the design and off-design conditions, respectively. The present volute pump include the impeller, volute, and discharge pipe. Important flow phenomena are described in detail from LES, and they are compared with those from URANS. From this comparison, we suggest what flow phenomena URANS can and cannot predict for flow inside a pump, and when and why LES is required for this flow.

Chapter 2

Numerical details of URANS

The detailed information on the pump specification and computational setup of the LES are given in part I. Therefore, in this chapter, we only provide explanation on the computational setup of the URANS. For URANS, we use a commercial software (Ansys CFX 2020 R1) with $k-\omega$ SST turbulence model (Menter 1994), in which unstructured grids are used. Second-order backward Euler method is used for temporal integration. For spatial discretization, high resolution scheme (Barth & Jespersen 1989; ans 2020) is used. The scheme uses non-linear blending function such that the discretization behaves like central difference in regions with low gradients and upwind difference in regions with high gradients. In URANS, the same computational domain size as LES is adopted (i.e., $-0.36 \leqslant x/R_2 \leqslant 1.74$, $r/R_2 \leqslant 6$, and $0 \leqslant \theta \leqslant 2\pi$ in the axial, radial, and azimuthal directions, respectively). However, in URANS, the computational domain is divided into a rotating zone enclosing the impeller and a stationary zone including the rest. The reference pressure is defined at the center of the duct inlet same as LES. For boundary conditions, Dirichlet

boundary condition with a uniform velocity profile is imposed at the inlet and average static pressure is set to zero at the outlet. Although the average outlet pressure is assigned zero for URANS, the reference pressure is defined at the center of the duct inlet same as LES for analysis. $\mathbf{u} = \boldsymbol{\Omega} \times \mathbf{x}$ and $\mathbf{u} = 0$ are applied on the rotating and stationary surfaces, respectively.

Chapter 3

Results and discussions

3.1. Resolution studies and comparison to experiments

The detailed explanation for the resolution study on LES is given in part I. Thus, we mainly provide information on URANS resolution study with comparison to LES. For the adequacy of grid resolution, we test four and three grid systems for LES and URANS, respectively (Table 3.1). The finest meshes (LES4 and URANS3) have approximately 512 million and 13 million grids, respectively.

In URANS, steady simulation is first carried out with a frozen rotor interface, where the relative position between the impeller and volute casing is fixed. Once steady simulation converges, unsteady simulation starts. A transient rotor-stator model is applied to consider the relative motion between the impeller and volute casing in the unsteady simulation. URANS simulation is performed at $\Delta t U_2/R_2 = \pi/1000$ (corresponding to 2,000 time steps per impeller revolution) which is comparable to the temporal resolution of LES (i.e., $\Delta t U_2/R_2 = \pi/1500$ for LES3). 512 processors (Intel Xeon Phi 7250) and 20 processors (Intel Xeon 6148) at the

KISTI supercomputing center are utilized for MPI parallel computations of LES and URANS, respectively.

To verify the results from numerical simulations, their head coefficient and efficiency are compared with experimental data. The detailed information on experiments is given in part I. Fig. 3.1 shows the head coefficient and efficiency from LES and URANS at the design and off-desgin conditions ($\phi_{\mathrm{d}} = 0.0845$ and $\phi_{\mathrm{off}} = 0.0483$, respectively), together with those by experiments. In URANS, the pump performances little vary with grid resolution, and do not match the experimental ones very well. However, in LES, they converge to experimental ones with increasing grid resolution. The agreements of the pump performances by LES are excellent even for the off-design condition. With LES3, differences in two parameters are less than 1% for the design condition. At the off-design condition, the differences in the head coefficient and efficiency is about 1% and 4%, respectively. URANS overpredicts the pressure rise even at the design condition, and thus overestimate the efficiency. For example, with URANS3, the differences in the head coefficient and efficiency are about 11% and 20% at the design condition, respectively, and approximately 4% and 16% at the off-design condition, respectively. It is interesting to note that the prediction by URANS at the design condition is worse than that at the off-design condition for the present problem. Since the pump performances by LES3 are nearly the same as those by LES4, we present the results from LES3 in the following. We also present results from URANS3, to see how LES predicts flow differently from URANS.

3.2. Flow near the interface between the impeller blade and volute

Fig. 3.2 shows the contours of the instantaneous and phase-averaged vorticity magnitude at the volute mid-span for the design and off-design conditions by LES and URANS, respectively. The phase averaging is performed as

$$\langle f(\mathbf{x},t)\rangle = \frac{1}{N}\sum_{n=0}^{N-1} f(\mathbf{x}, t+\frac{2\pi n}{N_b\Omega}), \tag{3.1}$$

where $f(\mathbf{x},t)$ is a flow variable. The contour levels of the instantaneous flow fields by LES are different from those of the phase-averaged ones by LES and of the instantaneous ones by URANS, because the first is much stronger than the latter. Solid black circles near the impeller tip in URANS (Fig. 3.2(c) and (f)) indicate the interface between the rotating and stationary frames. Due to interpolation errors evolved from this interface, solutions are locally discontinuous there. In LES, we solve governing equations in a single frame of reference using the immersed boundary method (Kim & Choi 2006), thus no interpolation errors at such interface occur. Advantages of immersed boundary methods in simulations of complex turbomachinery flows were well clarified in the previous literature (Posa *et al.* 2011).

Let us first discuss the instantaneous vorticity fields obtained by LES. For the design condition (Fig. 3.2(a)), trailing vortices are shed from the rotating blade, and the vortices near the blade suction surface advect downstream and interact with the trailing vortices in the volute. At the off-design condition (Fig. 3.2(d)), the vortices from the blade suction surface are much weaker than those observed for the design condition due to the lower mean flow rate. Nonetheless, the vortices shed from the blade

trailing edge are quite strong, convect more in the azimuthal direction than those of the design condition, and interact with the ones from the next blade, creating a wider distribution of strong vortices in the volute (see also part I and Kye *et al.* 2018).

Now, let us discuss the phase-averaged vorticity field by LES. For both design and off-design conditions (Figs. 3.2(b) and (e)), strong vorticity is observed only near the trailing edges of the blades and do not appear in the volute region, which is significantly different from the instantaneous vorticity fields. This is because vortices from the blade trailing edge are shed irregularly in the radial direction and thus the averaged vorticity becomes much weaker than the instantaneous ones. It is interesting to note that the phase-averaged vorticity fields are rather similar to those by URANS (Figs. 3.2(c) and (f)), indicating that URANS may provide phase-averaged flow features to some degree. However, it is clear that URANS completely miss the instantaneous nature of turbulent flow in the impeller and volute.

The strong vortices in the volute induce considerable turbulent kinetic energy inside the pump (Fig. 3.3). The instantaneous turbulent kinetic energy fields are drawn instead of the phase-averaged turbulent kinetic energy fields to explore the instantaneous nature of turbulent flow as explained above. The fluctuating velocity u' is computed by subtracting the phase-averaged velocity $\langle u \rangle$ from the instantaneous velocity u (i.e., $u' = u - \langle u \rangle$). It is clear trailing vortices from the rotating blade and vortices from the blade suction surface induce highly turbulent flows inside the impeller and volute. Turbulent kinetic energy is much stronger at the off-design condition in the impeller as well as in the volute than those at the design condition indicating vortices for the former case are highly un-

steady. The present pump has higher fluctuations along the blade suction surface than along the pressure surface, agreeing with the previous results from three-dimensional centrifugal impellers (Posa *et al.* 2015, 2016; Pedersen *et al.* 2003; Feng *et al.* 2009*a*, 2011). Although there were previous studies reporting higher fluctuations along the blade pressure side than along the suction side of centrifugal impellers (Abramian & Howard 1994; Ubaldi *et al.* 1998), their experiments did not consider volute casings thus neglecting the impeller-volute interaction.

3.3. Flow characteristics inside the impeller

We investigated the flow characteristics inside the impeller simulated by LES in part I. In this section, we compare the flow characteristics by LES and URANS inside the impeller. The blade centerline coordinate is introduced again as in part I (Fig. 3.4). Blades are numbered from 1 to 5 in the clockwise direction, where the blade 1 is the first blade from the volute tongue (Fig. 3.4(b)). The reduced pressure and skin-friction coefficients are defined as

$$C_{p_r} = \frac{\langle p \rangle - 0.5\rho\Omega^2 r^2 - p_\infty}{0.5\rho U_2^2}, \quad C_f = \frac{\tau_w}{0.5\rho U_2^2}, \tag{3.2}$$

where $\tau_w (= \mu \partial \langle w_s \rangle / \partial n)$ is the wall shear stress along the blade centerline, w_s is the velocity in the s direction, p_∞ is the pressure at the center of the pump inlet, $\langle\rangle$ denotes the phase averaging, and n is the surface-normal direction.

Before we compare the wall flow characteristics by LES and URANS, we examine flow sturctures inside the impeller passage briefly. Fig. 3.5 displays the instantaneous streamlines (based on the relative velocity) inside the impeller passage (near the volute tongue) together with the contours

of the instantaneous radial velocity for two flow rates. The instantaneous radial velocity are drawn by two color (red and blue) contours for positive and negative vales, respectively. The blue areas on streamlines exhibit about half of separation bubbles near the impeller surface. At the design condition, small ("A") and large ("B") recirculated zones are found along the blade suction and pressure sides, respectively. For the off-design condition, stronger and larger recirculated zone ("B") is observed than that for the design condition, and another separation bubble ("C") forms on the blade suction side. The strong impeller-volute interaction for the off-design condition induces highly unsteady flow separation on the blade pressure surface with much larger separation bubble near the tongue (see also part I and Kye *et al.* 2018).

The detailed characteristics of the wall pressure and skin-friction coefficient by LES for the design and off-design conditions is explained in part I. Thus, in this section, we focus on the comparison of the wall pressure and skin-friction by LES and URANS. Fig. 3.6 shows the reduced pressure and skin-friction coefficients computed by LES and URANS for the design condition. The agreement between the two numerical methods is relatively good. Along the pressure surface, Both LES and URANS captures adverse pressure gradient after the blade leading edge and favorable pressure gradient before the trailing edge. A relatively large separation bubble ("B" in Fig. 3.5(a)) is also represented by both numerical methods. Along the suction surface, steep adverse pressure gradient and a small separation bubble ("A" in Fig. 3.5(a)) are observed, followed by the moderate skin friction variation. The similar flow characteristics of the wall pressure and skin-friction between five blades is well predicted by LES and URANS with the exception of the pressure along the blade pressure

side near the tongue. For the blade near the tongue, larger pressure gradient is induced inside the passage due to the blade-tongue interaction. The skin-friction at the trailing edge of the blade pressure side by URANS demonstrates somewhat unrealistic drop because of the interpolation error between the two different computational domains (i.e., rotating and stationary).

Fig. 3.7 shows the reduced pressure and skin-friction coefficients computed by LES and URANS for the off-design condition. The similarity between the five blades are not conserved at the off-design condition. A large amount of fluid leaks to the volute upstream part through the impeller-tongue gap forming high pressure region near the trailing edge and much larger separation bubble ("B" in Fig. 3.5(b)) along the blade near the tongue. In LES, this results in the clear difference for the blade near the tongue from the other four blades. The evolution of the wall pressure and skin friction along the other four blades show very similar characteristics each other. However, URANS does not resolve the difference between the blade near the tongue and the other four blades. The pressure and skin friction along the five blades show very different aspect each other. Along the blade pressure side near the tongue, URANS also exhibits high pressure but this is largely underpredicted compared with that by LES. The larger separation bubble along the blade near the tongue is not observed in URANS. Moreover, no flow separation occurs along the centerline of the blade 3 for both blade pressure and suction sides. This comparison shows URANS predicts the evolution of the wall pressure and skin friction along the blade centerline well at the design condition but not at the off-design condition.

So far, we have visited the flow characteristics along the blade cen-

terline coordinate s. Although it reveals detailed information along the blade surface, overall flow features in the impeller passage are hardly predictable. Therefore, we investigate radial velocity distribution at constant radius $r/R_2 = 0.7$ between the blade 1 and 5 simulated by LES and URANS in Fig. 3.8. The radial position corresponds to the blade centerline coordinate $s = 0.63$ approximately. Blade-to-blade flow fields of LES and URANS display similar radial velocity distribution even for the off-design condition. However, unsteady nature of turbulent flow inside the impeller passage is not fully resolved in the URANS. Rather, URANS exhibits similar velocity distribution to the phase-averaged flow fields of LES. Higher radial velocity for the blade suction side and lower radial velocity for the blade pressure side are observed following the potential flow effect of the relative eddy explained in part I. Low and even negative radial velocity region is induced on the blade pressure side due to the large separation bubble there. Although URANS does not fully resolve instantaneous feature of turbulent flow, it captures overall velocity distribution well inside the impeller passage for both flow conditions.

3.4. Radial thrust and pressure fluctuations along the impeller periphery

The radial thrust is the force acting on an impeller in the radial direction (Brennen 1994). In a volute-type centerifugal pump, the radial thrust is generated due to the interaction between rotating and stationary parts. This force may lead to shaft failure due to fatigue (Agostinelli *et al.* 1960) and high levels of vibration and noise (van Esch 2009). Thus, an accurate prediction of the mean and maximum radial thrusts is important. Fig. 3.9 shows the instantaneous and mean radial thrusts, together with root-

mean-square (rms) thrust fluctuations on the polar diagram. The volute angle ξ is defined as the azimuthal angle in a clockwise direction from the volute tongue (i.e., zero at the tongue), denoting the direction of the radial thrust. The distance from the origin represents the magnitude of the thrust.

At the design condition, weak radial thrust is imposed to the impeller, whereas that at the off-design condition, which is about 57% of the design flow rate, becomes much stronger and is directed toward the volute upstream. This strong radial thrust toward the volute upstream for the off-design condition results from rapid pressure rise in the volute and subsequent nonuniform pressure distribution in the azimuthal direction (Agostinelli *et al.* 1960; Baun & Flack 1999; Barrio *et al.* 2011). Strong impeller-volute interaction at the off-design condition causes highly unsteady radial thrust. Hence, stronger fluctuations of radial thrust are observed. Although fluctuations of the radial force are relatively well preserved, the instantaneous and mean radial thrust are largely underestimated in URANS. The underestimation of the radial thrust can lead to false design of the impeller and early fatigue failure. Therefore, it is wise to adopt LES for pumps of which the radial thrust is important design consideration.

To our knowledge, there has been no study comparing pressure pulsations predicted by LES and URANS in centrifugal pumps. Thus, we measure pressure along the impeller periphery and perform the triple decomposition (Hussain & Reynolds 1970; Reynolds & Hussain 1972) of the instantaneous pressure as follows:

$$p(\mathbf{x}, t) = \bar{p}(\mathbf{x}) + \hat{p}(\mathbf{x}, t) + p'(\mathbf{x}, t) \tag{3.3}$$

where $\bar{p}, \hat{p}, p'$ are the time-averaged value, contribution of the organized wave, and contribution of the turbulence, respectively. Then, the periodic wave component is computed by:

$$\hat{p} = \langle p \rangle - \bar{p} \tag{3.4}$$

where the phase average is defined by the equation 3.1. To investigate pressure fluctuations in LES and URANS, we measure pressure at constant $r/R_2 = 1.03$ on the volute mid-span as seen in Fig. 3.4(b). The pressure signal is collected during 100 revolutions on LES3 and 20 revolutions on URANS3. In the present study, we obtain a fluctuating pressure p which is filtered in space for LES and ensemble-averaged for URANS. As noted by previous studies (Hussain & Reynolds 1970; Reynolds & Hussain 1972), fluctuating components of the periodic motion and turbulence are uncorrelated, thus following is satisfied:

$$\overline{\hat{p}^2} + \overline{p'^2} = \overline{(\hat{p} + p')^2} = \overline{(p - \bar{p})^2} \tag{3.5}$$

The results are provided in Fig. 3.10. Pressure fluctuations by LES are examined in part I. Therefore, we focus on comparing those by LES and URANS in this part. For the design condition, fluctuations by the periodic blade rotation are larger than turbulent fluctuations even near the tongue, hence total fluctuations are mainly determined by contribution of the periodic fluctuation. In URANS, agreement in periodic fluctuations (in terms of the magnitude) is good but contribution of the turbulence is largely underpredicted. Thus, periodic and total fluctuations collapse in one curve. Also, the modulated distribution of the periodic component (see also part I) is not well maintained in URANS. Although LES shows five (i.e., the number of blades) peaks for periodic fluctuations, URANS

shows more peaks. At the off-design condition, turbulent fluctuations increase rapidly near the tongue by LES (not by URANS), and is dominant near the tongue. Total fluctuations are mainly determined by the turbulent fluctuations near the tongue and by both fluctuations elsewhere. Periodic contribution shows the modulated pattern along the circumference both in LES and URANS. In URANS, turbulent fluctuations are not negligible but still fairly underestimated especially near the tongue. Overall, URANS does not predict turbulent fluctuations for both flow condition. This is not surprising given that URANS solves the ensemble-averaged flow instead of the instantaneous flow. For the design condition, where turbulent fluctuations are small, URANS estimates total fluctuations well (in terms of magnitude). On the other hand, for the off-design condition near the tongue, URANS significantly underestimates total fluctuations owing to the inaccurate prediction for turbulent fluctuations.

3.5. Flow features inside the volute

So far, we have examined how the flow structures inside or around the impeller appear in LES and URANS. Here, we examine the flow characteristics in the volute simulated by two different numerical methods. Fig. 3.11 presents the contours of vorticity magnitude at the volute mid-span for the near-tongue region at the design and off-design conditions. Again, different contour level is adopted for instantaneous flow fields of LES. At the design condition (Fig. 3.11(a)), vortices shed from the blade trailing edge and near-wall vortices along the blade suction side are identified. Relatively weak vorticity distribution develops near the volute tongue owing to the weak blade-tongue interaction. At the off-design condition (Fig. 3.11(d)), strong vortices in broader areas are found along the vo-

lute. Vortices near the tongue interact with boundary layer flows near the trailing edge of the rotating blade. A large amount of volute fluid enters into the volute upstream causing considerable flow separation and vortices (see also part I). This induces high vorticity magnitude and high pressure fluctuations near the tongue (Fig. 3.10(b)). The phase-averaged vorticity fields for both flow conditions (Fig. 3.11(b) and (e)) identify overall features of the instantaneous flow fields. Strong vorticity magnitudes along the blade suction side, blade trailing edge and volute tongue are observed. At the design condition (Fig. 3.11(c)), URANS displays strong vorticity magnitudes at the tongue along the side of the discharge pipe, which implies that the incidence angle of the flow to the tongue is predicted differently from that by LES. The vorticity magnitude at the blade trailing edge is also underpredicted. At the off-design condition (Fig. 3.11(f)), somewhat unrealistic vorticity distribution is found along the impeller periphery (solid black line) due to the interpolation error between rotating and stationary domains.

Although URANS does not resolve instantaneous nature and turbulent fluctuations of unsteady flows in a centrifugal pump, it has been shown to provide reasonable agreement with phase-averaged flow fields of LES inside the impeller and volute. We further extend comparative analysis to time-averaged total pressure along the volute, which is one of the most important flow variables in centrifugal pumps. To compare total pressure variation quantitatively, χ is defined by the equation 3.6 for the plane of the volute mid-span (see Fig. 3.12b). R_{volute} is the radial distance from the impeller axis to the volute wall at the volute mid-span. The time-averaged total pressure coefficient is also given in the equation. In LES, pressure and velocity are time-averaged in the inertial frame of the refer-

ence on LES3 grids for 10 revolutions, corresponding 30,000 timesteps. In URANS, solution is time-averaged on URANS3 grids for one revolution to calculate total pressure coefficients, corresponding 2,000 timesteps.

$$\chi = \frac{r - R_2}{R_{\text{volute}} - R_2}, \bar{C}_{p_t} = \frac{\bar{p} + 0.5\rho|\bar{\mathbf{u}}|^2 - p_\infty}{0.5\rho U_2^2} \tag{3.6}$$

Fig. 3.12 depicts time-averaged total pressure coefficients at the volute mid-span computed by LES and URANS. For the design condition, the overall agreement between LES and URANS is surprisingly good. Contours of the time-averaged total pressure coefficient also exhibit good agreement between LES and URANS inside the volute. The distribution of the total pressure shows monotonous variation inside the volute due to the weak impeller-volute interaction. Fluid discharged from the impeller travels inside the volute without severe losses.

On the other hand, for the off-design condition, considerable losses occur along the upstream portion of the volute in LES. This can be attributed to the flow separation and intense turbulent fluctuations near the volute tongue. URANS, which does not resolve strong turbulent fluctuations particularly near the tongue, overpredicts the time-averaged total pressure coefficient in the near-tongue region. Despite the discrepancy near the tongue, URANS shows good agreement with LES for the rest of the volute area. Contours of the total pressure coefficient also indicate URANS predicts total pressure rise in the present pump well inside the impeller and volute except for the near-tongue region. LES demonstrates substantial drop in the total pressure coefficient occurs in the upstream part of the volute.

To predict the mean flow quantities inside an impeller and a volute, URANS can be a good alternative for LES with significantly less compu-

tational cost except for the near-tongue region of the off-design condition. However, performance comparison of Fig. 3.1 reveals that URANS overpredicts pressure rise of the pump especially for the design condition. This implies appreciable losses occur inside the discharge pipe for the present pump.

3.6. Flow characteristics inside the discharge pipe

Most of previous studies have focused on investigating flow characteristics in an impeller and a volute, and flow in the discharge pipe is probably one of undisclosed areas in the centrifugal pump research. Although URANS does predict mean flow characteristics in the impeller and volute of the present pump to some degree, it overpredicts pressure rise of the present pump compared to LES and experiments (Fig. 3.1). To identify losses which are not resolved in URANS, we inspect flow structures in the discharge pipe simulated by LES and URANS.

Fig. 3.13 demonstrates schematic diagram of the present pump and discharge pipe. The cross-sectional area of the discharge pipe increases from the volute throat to the discharge flange. The pump flow travels through the curved discharge pipe. The geometry with curvature and increasing cross-sectional area is expected to develop complex flow phenamena and losses in the discharge pipe. The variable ζ is defined as the distance of the straight pipe from the discharge flange. The Reynolds numbers based on the mean streamwise velocity and pipe diameter are about 250,000 and 140,000 for the design and off-design conditions, respectively.

Fig. 3.14 reveals the time-averaged streamlines and contours of the streamwise velocity inside the discharge pipe. LES and URANS flow fields

exhibit clear differences. At the design condition, LES shows large-scale swirl flows developing after the curved part of the discharge pipe. Flow separation is observed at $\zeta/D_{\mathrm{pipe}} = 0$ caused by the strong curvature and expansion. This flow separation contributes to the strong swirls which is much stronger than typical secondary flows developing inside the pipe bend. The contours of the streamwise velocity also display the influence of the curvature. Low velocity region forms at the inner part of the curvature and high velocity regions are observed at the outer part of the curvature. The streamwise velocity shows distorted distribution caused by the curvature and subsequent swirls. At the off-design condition, flow separation becomes weaker owing to the low mean flow rate. However, intense swirl flows still develops inside the discharge pipe as indicated by the three-dimensional streamlines. Contours of the streamwise velocity also demonstrate distorted distribution.

On the other hand, URANS does not predict flow separation and strong swirls caused by the curvature and expansion ratio of the discharge pipe. Smooth streamlines and homogeneous velocity distribution are observed inside the discharge pipe compared to those of LES for both flow rates. Although pumped fluid moves through the curved pipe with substantial expansion ratio, flow fields of URANS are not largely affected by the geometrical effects.

To compare losses occurring in the discharge pipes quantitatively, we present the area-averaged total pressure coefficients along ζ in Fig. 3.15. The time-averaged total pressure is area-averaged along the cross-section. Strong swirls originated from the diverging discharge pipe with curvature produce significant losses in LES. At the design condition, stronger swirls and larger losses occur due to higher flow rates than that at the off-design

condition. The total pressure drops inside the discharge pipe significantly.

On the other hand, URANS does not capture strong swirl flows and consequent losses in the discharge pipe. The total pressure of URANS deviates from that of LES as fluid travels further downstream. Furthermore, pressure drop predicted by the Darcy friction factor for the smooth straight pipe collapse well with those of URANS results, indicating the effect of the curvature and area expansion is nearly disregarded. The discrepancy between LES and URANS for the design condition, where larger losses arise due to higher mean flow rate, is larger than that for the off-design condition. To our knowledge, this is the first research reporting large-scale swirl flows and subsequent losses in a discharge pipe of a centrifugal pump. This is because URANS has been dominantly used in pump research and most experiments have focused on examining flows in impellers and volutes. Centrifugal pumps including diverging discharge pipes with strong curvatures should be carefully designed and examined by high-fidelity simulation like LES.

	$N_x \times N_r \times N_\theta$
LES1	$193 \times 433 \times 768$
LES2	$257 \times 481 \times 1024$
LES3	$257 \times 641 \times 1536$
LES4	$385 \times 769 \times 1728$
	Number of total mesh elements
URANS1	3,284,644
URANS2	6,505,524
URANS3	12,675,688

Table 3.1: Grid systems of LES and URANS

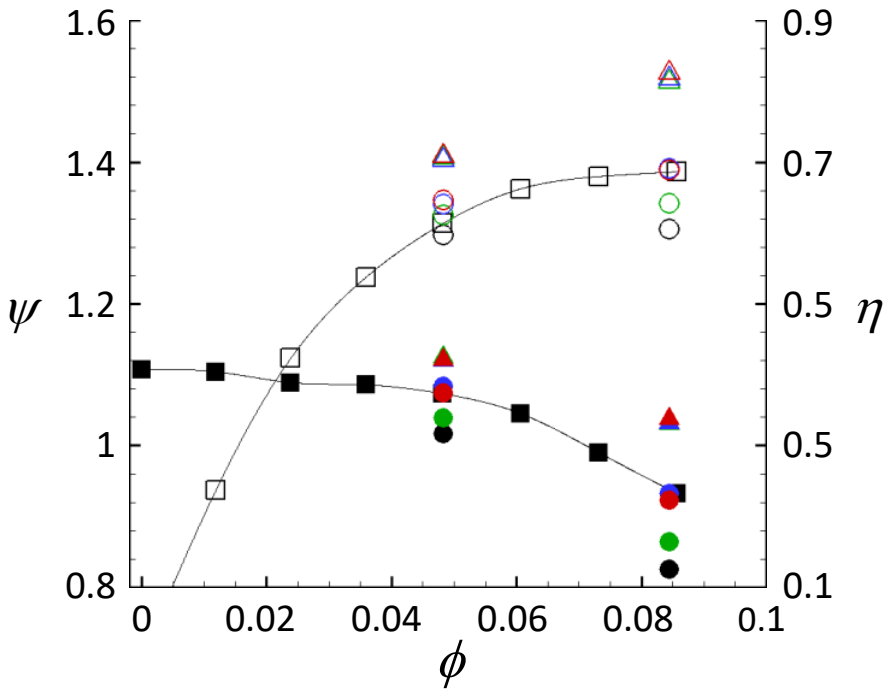

Figure 3.1: Pump performances versus flow coefficient: (□, ■) experiments; (○, ●) LES1; (○, ●) LES2; (○, ●) LES3; (○, ●) LES4; (△, ▲) URANS1; (△, ▲) URANS2; (△, ▲) URANS3. Solid and open symbols denote the head coefficient and efficiency, respectively.

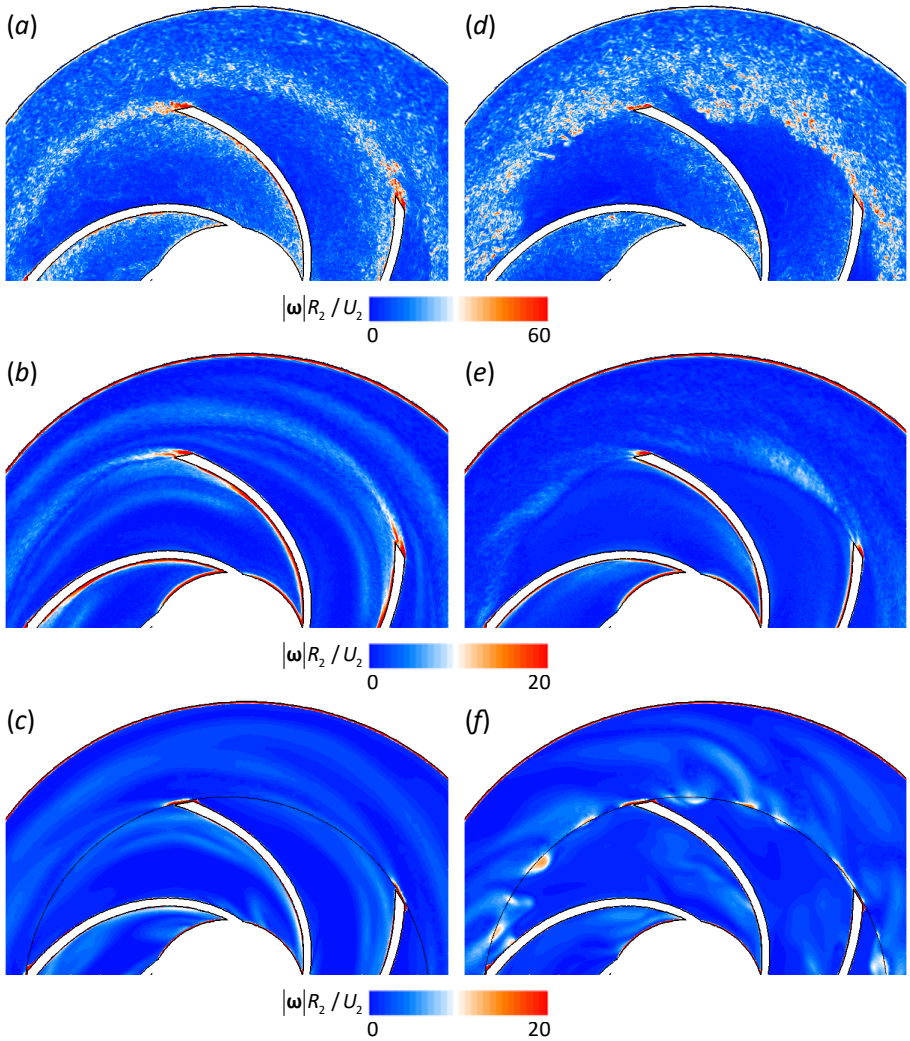

Figure 3.2: Contours of the vorticity magnitude at the volute mid-span on window W2 (Fig. 2.1(b) in part I) predicted by LES3 (a, b, d, e) and URANS3 (c, f) for the design (left) and off-design (right) conditions: (a, d) instantaneous flow; (b, e) phase-averaged flow; (c, f) instantaneous flow

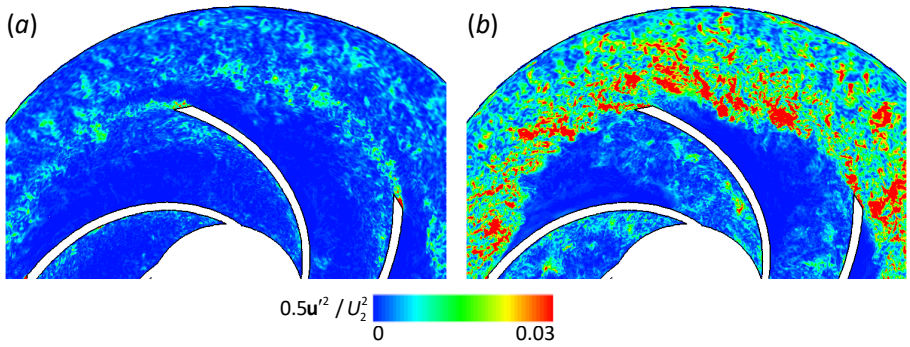

Figure 3.3: Contours of the instantaneous turbulent kinetic energy by LES3 at the volute mid-span on window W2: (a) design condition; (b) off-design condition

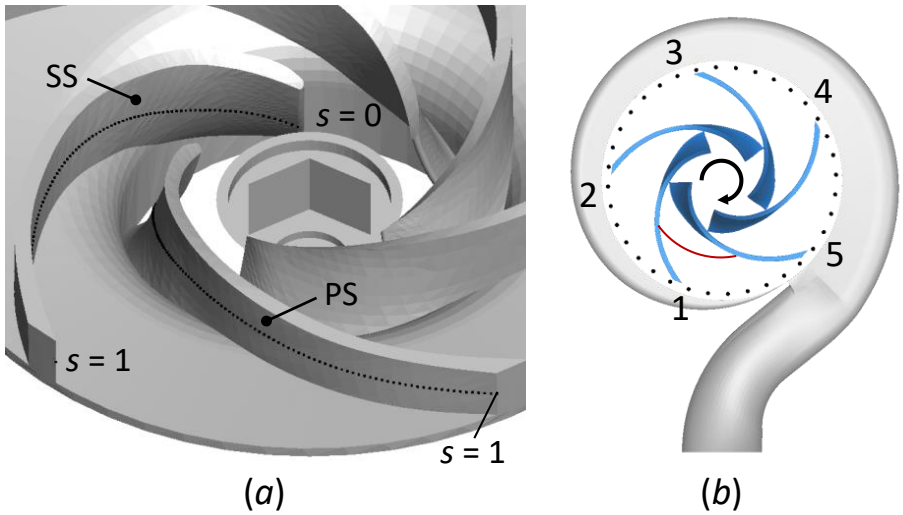

Figure 3.4: Blade centerline coordinate s and impeller blades 1-5 for the blade position angle of $\varphi = 54°$. In (a), PS and SS represent the blade pressure and suction surfaces, respectively. In (b), the red arc between blades 1 and 5 corresponds to $r/R_2 = 0.7$, and 36 black dots denote monitoring positions at $r/R_2 = 1.03$.

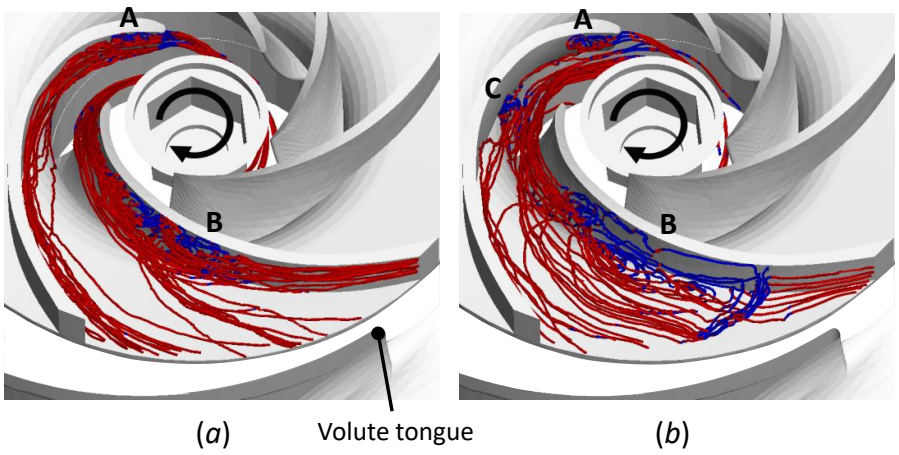

Figure 3.5: Instantaneous streamlines inside the passage near the tongue (between blades 1 and 5 of Fig. 3.4(b)) for the design (top) and off-design (bottom) conditions. Here, red and blue colors of the streamlines represent positive and negative radial velocities, respectively.

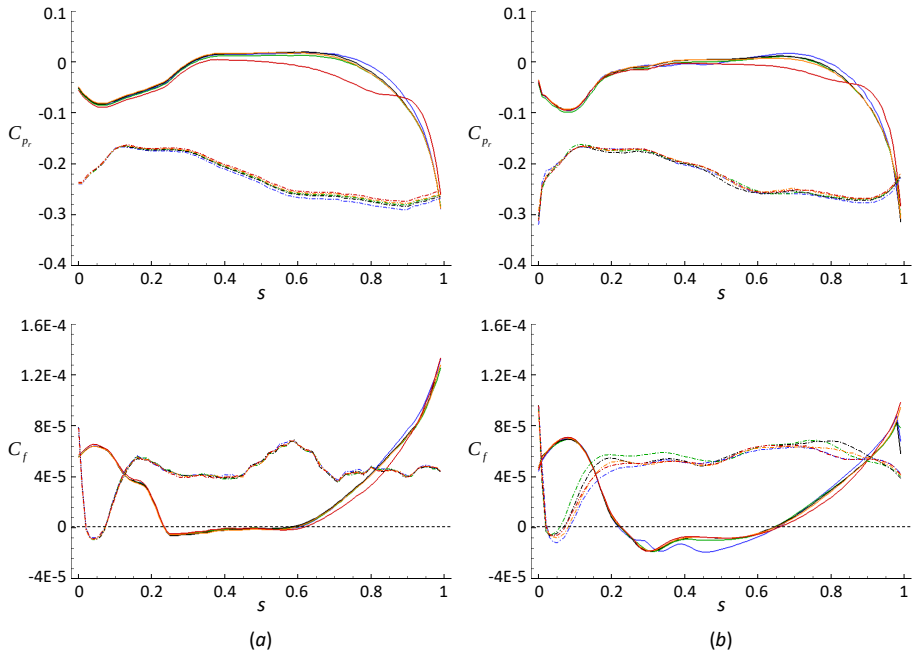

Figure 3.6: Reduced pressure (top) and skin-friction (bottom) coefficients ($\varphi = 54°$) for the design condition: (a) phase-averaged flow by LES; (b) instantaneous flow by URANS. ——— along the pressure side; - - - -, along the suction side; ———, blade1; ———, blade2; ———, blade3; ———, blade4; ———, blade5.

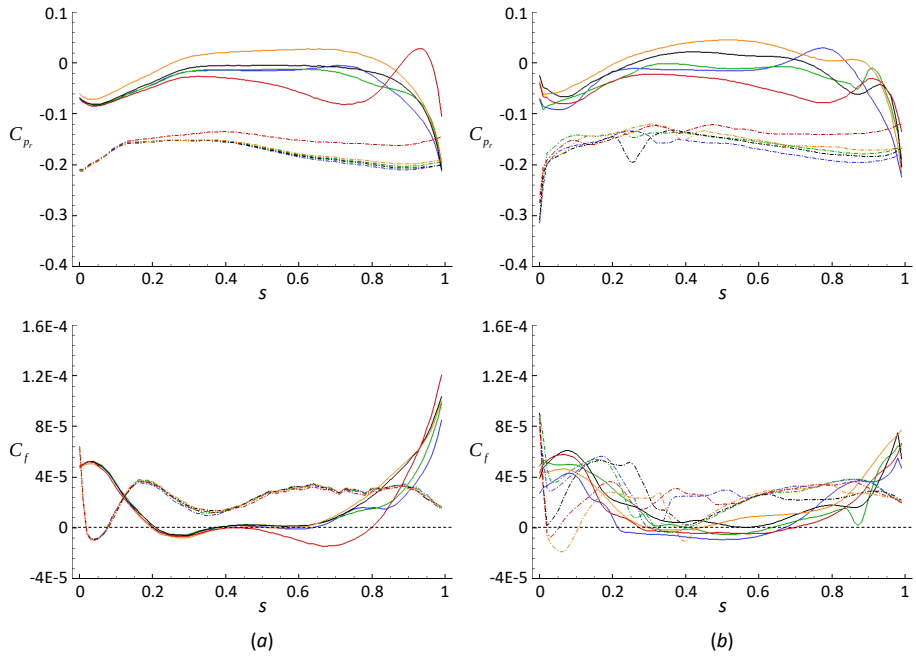

Figure 3.7: Reduced pressure (top) and skin-friction (bottom) coefficients ($\varphi = 54°$) for the off-design condition: (a) phase-averaged flow by LES; (b) instantaneous flow by URANS. ——— along the pressure side; - - - -, along the suction side; ———, blade1; ———, blade2; ———, blade3; ———, blade4; ———, blade5.

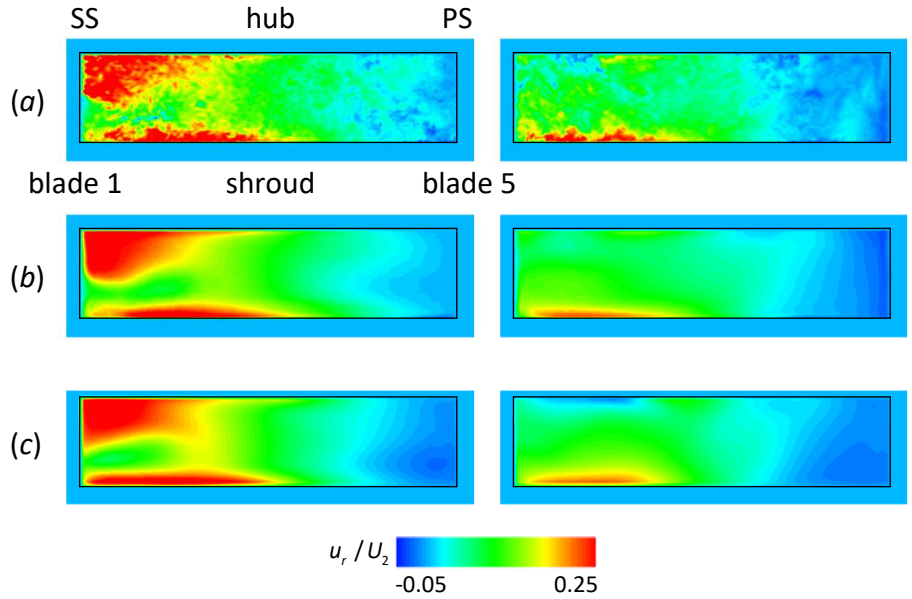

Figure 3.8: Contours of the radial velocity along the constant radius $r/R_2 = 0.7$ (Fig. 3.4(b)) between the blade 1 and 5 predicted by LES (a, b) and URANS (c) for the design (left) and off-design condition (right): (a, c) instantaneous flow fields; (b) phase-averaged flow fields. The blade position angle is $\varphi = 54°$

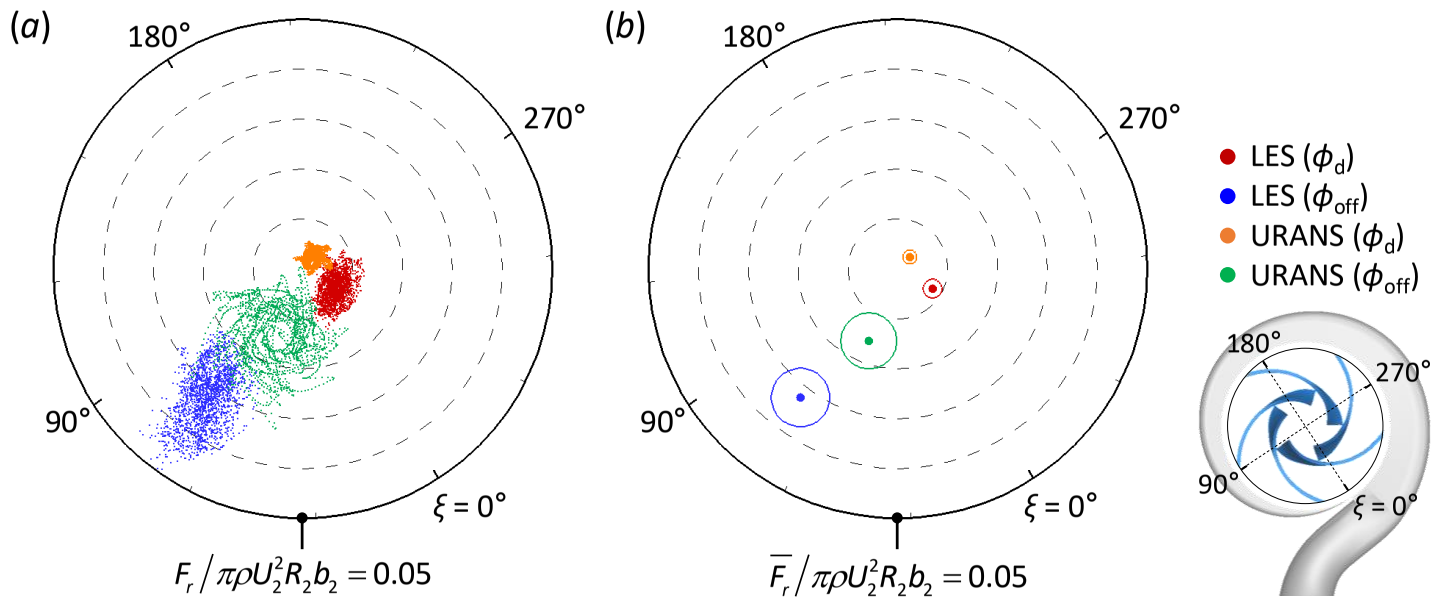

Figure 3.9: Polar representation of the radial thrust on the impeller for 10 impeller revolutions: (a) instantaneous thrust; (b) time-averaged thrust (solid circle) and rms thrust (radius of the surrounding circle). In (a), 2,000 instantaneous radial thrusts are shown (i.e., every 15th and 10th instantaneous thrusts are drawn for LES and URANS, respectively.

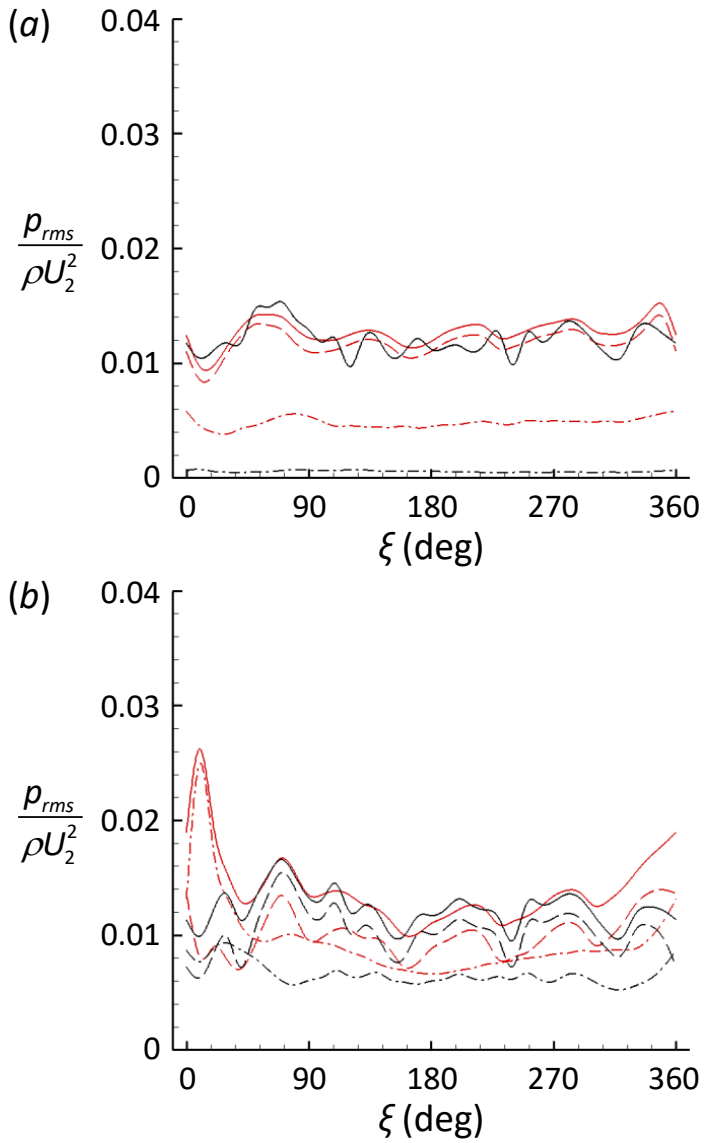

Figure 3.10: Pressure pulsations at constant radius $r/R_2 = 1.03$ on the volute mid-span computed by LES (red) and URANS (black): - - - -, fluctuations of periodic motion ($\hat{p}$); - · - · -, turbulent fluctuations (p'); ——— total fluctuations ($\hat{p} + p'$). (a) design condition; (b) off-design condition.

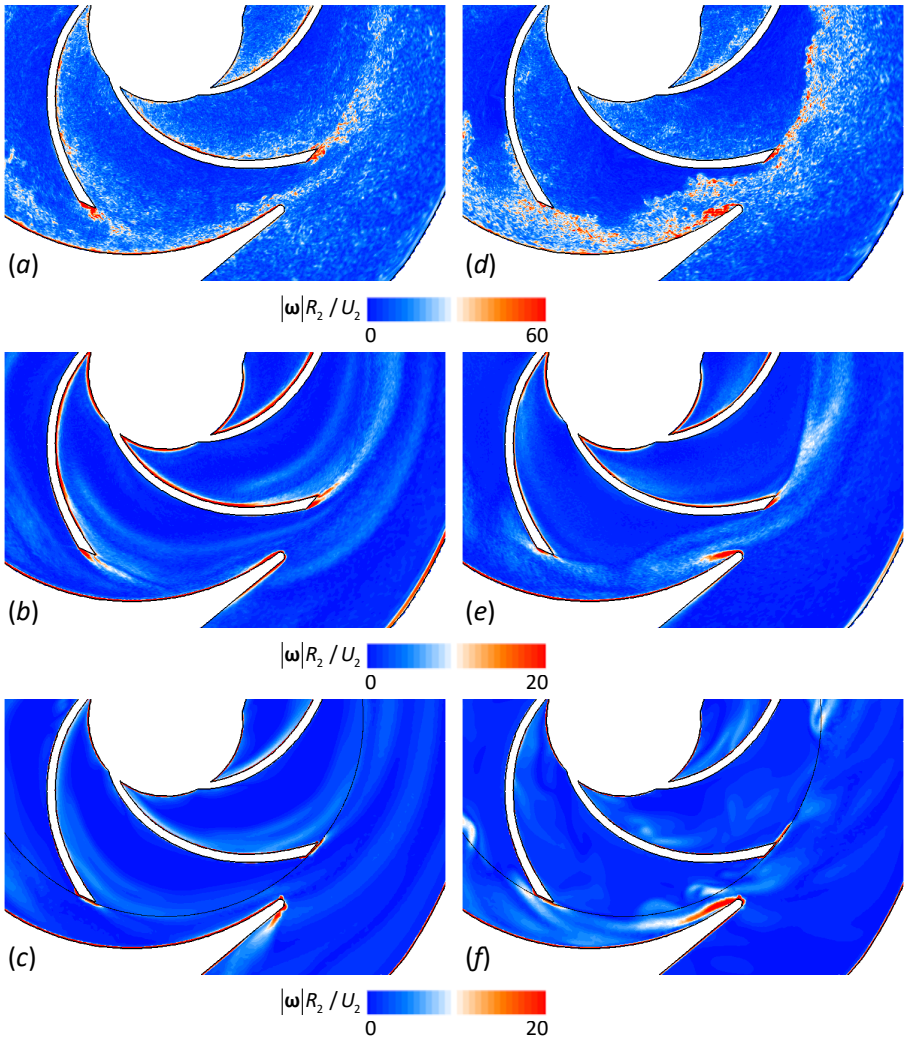

Figure 3.11: Contours of vorticity magnitude at the volute mid-span on window W1 (Fig. 2.1(b) in part I) predicted by LES (a, b, d, e) and URANS (c, f) for the design (top) and off-design (bottom) conditions: (a, d) instantaneous flow fields; (b, e) phase-averaged flow fields; (c, f) instantaneous flow fields

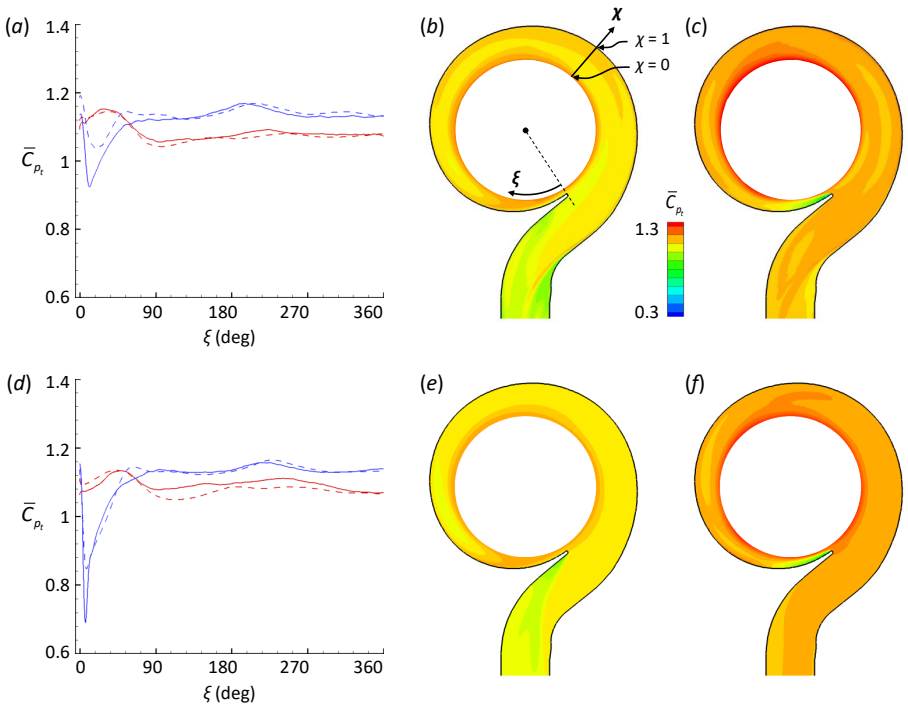

Figure 3.12: Evolution of the time-averaged total pressure along the volute angle (a, d), and contours of the time-averaged total pressure (b, c, e, f) at the volute-midspan: (a) $\chi = 0.5$; (d) $\chi = 0.75$; (b) design condition in LES; (c) off-design condition in LES; (e) design condition in URANS; (f) off-design condition in URANS. In (a, d), results of the design and off-design conditions are described by red and blue, respectively. The solid and dashed lines represents LES and URANS results, respectively.

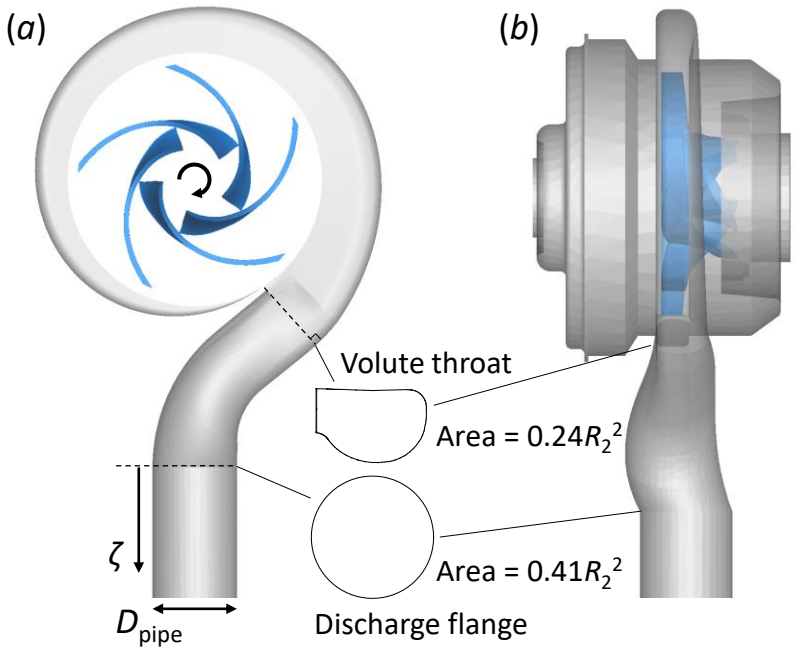

Figure 3.13: Schematic diagram of the pump and the discharge pipe: (a) top view; (b) side view. Only blades are shown in the impeller.

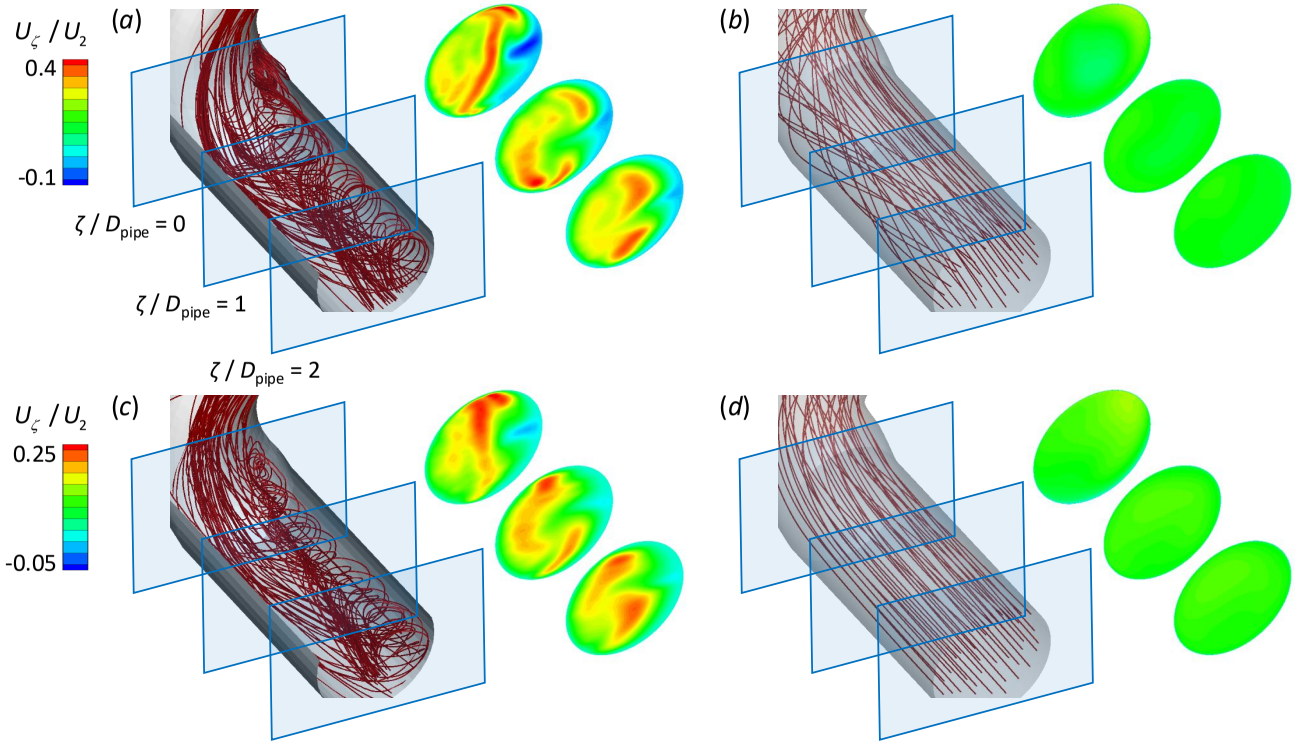

Figure 3.14: The time-averaged streamlines inside the discharge pipe and contours of the time-averaged streamwise velocity at $\zeta/D_{\text{pipe}} = 0, 1,$ and 2 predicted by LES (a, c) and URANS (b, d) for the design (top) and off-design (bottom) conditions

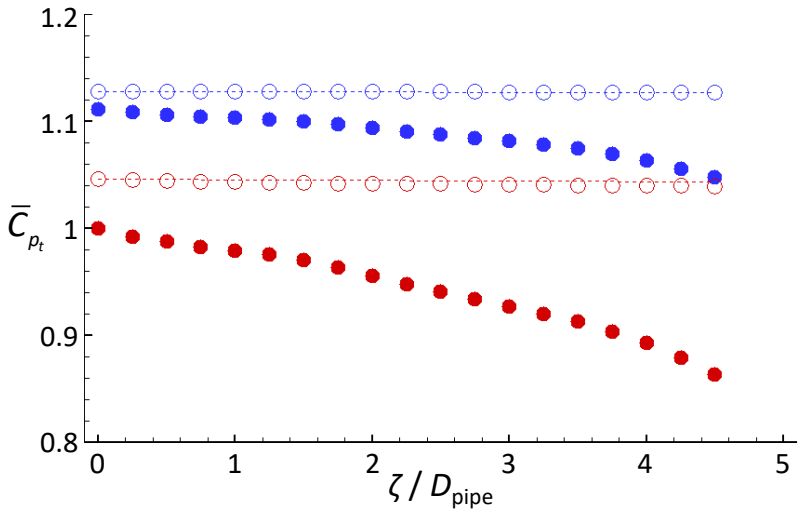

Figure 3.15: The area-averaged total pressure coefficients along ζ for the design (red) and off-design (blue) conditions. Solid and open circles indicate results of LES and URANS, respectively. The dashed line denotes pressure drop in the smooth straight pipe predicted by the Darcy friction factor.

Chapter 4

Summary and concluding remarks

In this paper, we performed LES and URANS computations to investigate turbulent flows in a volute-type centrifugal pump. We considered two flow conditions: the design (ϕ_{d}) and the off-design ($\phi_{\mathrm{off}} = 0.57\phi_{\mathrm{d}}$) conditions. The Reynolds number of the pump is 1,740,000 based on the blade tip velocity and radius of the impeller blade. LES was conducted in a single reference frame, i.e., the non-inertial reference frame, with an immersed boundary method. In URANS, rotating and stationary computational domains were used to simulate flows in the impeller and elsewhere, respectively. This resulted in local discontinuity in the vorticity field at the interface between two domains. LES predicted the pressure rise and efficiency of the pump accurately, while URANS showed considerable differences with experiments. Flow characteristics inside the impeller, volute, and discharge pipe was compared thoroughly between LES and URANS.

URANS did not resolve instantaneous nature of turbulent flows in the volute pump. The instantaneous flow field of LES exhibited small-scale

turbulent structures of vortices shed from the blade trailing edge and developing along the boundary layer flow of the blade suction surface. The vorticity field for the off-design condition showed stronger magnitude in extensive volute area than that for the design condition due to strong impeller-volute interaction for the former condition. The phase-averaged vorticity fields showed much weaker vorticity distribution than that by the instantaneous vorticity fields becuase of irregulary shed vortices from trailing edges of blades. URANS demonstrated similar traits to the phase-averaged flow field of LES, indicating that it provides phase-averaged flow features to some degree. Therefore, URANS missed the instantaneous nature of turbulent flow in the impeller and volute.

Inside the impeller passage, the reduced pressure and skin-friction along the blade centerline were investigated. Adverse pressure gradient developed along the blade surface generating separation bubbles especially for the blade pressure side. For the design condition, wall flow characteristics showed similar characteristics between five blades. These characteristics were also well identified by URANS. On the other hand, for the off-design condition, pressure and skin friction on the blade pressure side near the tongue displayed different aspect presenting larger separation bubble than along the other four blades. However, URANS showed different characteristics between each blades. Larger separation bubble, along the blade pressure side near the tongue, and similarity between the other four blades were not found.

Also, URANS did not predict the radial thrust and turbulent fluctuations along the impeller periphery. Although URANS predicted the rms fluctuations of the radial thrust on the impeller, it substantially underestimated the mean and maximum thrust for both flow conditions.

This may lead to false design of the impeller and early fatigue failure. The triple decomposition of pressure fluctuations was conducted along the impeller periphery. For the design condition, the turbulent fluctuations were smaller than the periodic fluctuations even near the tongue. On the other hand, for the off-design condition, turbulent fluctuations increased significantly especially near the tongue. Compared with LES, URANS predicted periodic fluctuations well but largely underpredicted turbulent fluctuations. Therefore, URANS represented comparable total fluctuations with LES for the design condition but failed to predict pressure fluctuations accurately for the off-design condition.

Although instantaneous flow features and turbulent fluctuations were not accurately predicted in URANS, URANS captured mean flow characteristics inside the impeller and volute especially for the design condition. The blade-to-blade radial velocity distribution by LES and URANS showed similar distribution. Higher radial velocity on the blade suction side than that on the blade pressure side was represented by both numerical methods. Although instantaneous flow features were not managed in URANS, overall agreement between LES and URANS was satisfactory for both flow conditions. Inside the volute, the time-averaged total pressure coefficient was compared. URANS predicted the evolution of the total pressure coefficient inside the volute well at the design condition. At the off-design condition, significant losses occurred at the volute upstream because of flow separation at the tongue. URANS did not resolve these losses and overestimated the total pressure there. However, it showed good agreement with LES for the rest of the volute area.

The fluid exited the volute traveled through the curved and diverging pipe in the present pump. Because of the curvature and area expansion,

flow separation developed at the inner corner of the discharge pipe and the large-scale swirl flows grew creating considerable losses. The larger losses were observed for the design condition because of the higher mean flow rate. However, URANS failed to embrace the influence of the curvature and area expansion of the discharge pipe and overpredicted the pressure rise and efficiency consequently.

In the present study, we compared various turbulent flow characteristics inside the volute-type centrifugal pump by LES and URANS. Through this comparative study, we aimed to comprehend when LES is necessary or URANS is adequate. The study suggests that URANS can be a desirable tool to predict mean flow characteristics varying periodically by the impeller rotation, especially at the design condition. However, URANS does not accurately predict instantaneous nature and fluctuations of unsteady flows mainly because it does not resolve turbulent fluctuations. Thus, LES is necessary to investigate the instantaneous features and turbulent characteristics of flow such as unsteady flow separation inside the impeller at the off-design condition, flow separation at the tongue, pressure fluctuations, trailing vortices shed from rotating blades. Also, URANS inaccurately predicts even mean flow characteristics for highly unsteady flows like strong swirls in the discharge pipe and flow separation at the tongue.

References

2020 *ANSYS CFX-solver theory guide*. ANSYS Inc.

2020 Europump supports epa for energy use. *World Pumps* **2020** (2), 22–24.

Abramian, M. & Howard, J. H. G. 1994 Experimental investigation of the steady and unsteady relative flow in a model centrifugal impeller passage. *ASME J. Turbomach.* **116** (2), 269–279.

Agostinelli, A., Nobles, D. & Mockridge, C. R. 1960 An experimental investigation of radial thrust in centrifugal pumps. *ASME J. Eng. Power* **82** (2), 120–125.

Akselvoll, Knut & Moin, Parviz 1996 An efficient method for temporal integration of the navier–stokes equations in confined axisymmetric geometries. *J. Comput. Phys.* **125** (2), 454–463.

Alemi, H., Nourbakhsh, S. A., Raisee, M. & Najafi, A. F. 2015 Effects of volute curvature on performance of a low specific-speed centrifugal pump at design and off-design conditions. *ASME J. Turbomach.* **137** (4), 041009.

Asuaje, Miguel, Bakir, Farid, Kouidri, Smaïne, Kenyery, Frank & Rey, Robert 2005 Numerical modelization of the flow in centrifugal pump: volute influence in velocity and pressure fields. *Int. J. Rotating Mach.* **2005** (3), 244–255.

Barrio, Raúl, Blanco, Eduardo, Parrondo, Jorge, González, José & Fernández, Joaquín 2008 The effect of impeller cutback on the fluid-

dynamic pulsations and load at the blade-passing frequency in a centrifugal pump. *ASME J. Fluids Eng.* **130** (11), 111102.

Barrio, R., Fernández, J., Blanco, E. & Parrondo, J. 2011 Estimation of radial load in centrifugal pumps using computational fluid dynamics. *Eur. J. Mech. B-Fluids* **30** (3), 316–324.

Barrio, Raúl, Parrondo, Jorge & Blanco, Eduardo 2010 Numerical analysis of the unsteady flow in the near-tongue region in a volute-type centrifugal pump for different operating points. *Comput. Fluids* **39** (5), 859–870.

Barth, T. & Jespersen, D. 1989 The design and application of upwind schemes on unstructured meshes. *AIAA Paper 89-0366* .

Baun, D. O. & Flack, R. D. 1999 A plexiglas research pump with calibrated magnetic bearings/load cells for radial and axial hydraulic force measurement. *ASME J. Fluids Eng.* **121** (1), 126–132.

Beddhu, Murali, Taylor, Lafayette K. & Whitfield, David L. 1996 Strong conservative form of the incompressible navier–stokes equations in a rotating frame with a solution procedure. *J. Comput. Phys.* **128** (2), 427–437.

Boccazzi, A., Miorini, R., Sala, R. & Marinoni, Franco 2009 Unsteady flow field in a radial pump vaned diffuser. In *8th European conference on turbomachinery: fluid dynamics and thermodynamics*, pp. 1103–1112.

Brennen, C.E. 1994 *Hydrodynamics of Pumps*. Cambridge University Press.

Byskov, Rikke K., Jacobsen, Christian B. & Pedersen, Nicholas 2003 Flow in a centrifugal pump impeller at design and off-design conditions—part ii: large eddy simulations. *ASME J. Fluids Eng.* **125** (1), 73–83.

Cheah, Kean Wee, Lee, Thong See & Winoto, Sonny H. 2011 Unsteady analysis of impeller-volute interaction in centrifugal pump. *Int. J. Fluid Mach. Sys.* **4** (3), 349–359.

Chu, S., Dong, R. & Katz, J. 1995 Relationship between unsteady flow,

pressure fluctuations, and noise in a centrifugal pump—part b: Effects of blade-tongue interactions. *ASME J. Fluids Eng.* **117** (1), 30–35.

Dixon, S. L. & Hall, C. A. 2014 *Fluid Mechanics and Thermodynamics of Turbomachinery*. Butterworth-Heinemann.

Dong, R., Chu, S. & Katz, J. 1992 Quantitative visualization of the flow within the volute of a centrifugal pump. part b: Results and analysis. *ASME J. Fluids Eng.* **114** (3), 396–403.

Dong, R., Chu, S. & Katz, J. 1997 Effect of modification to tongue and impeller geometry on unsteady flow, pressure fluctuations, and noise in a centrifugal pump. *ASME J. Turbomach.* **119** (3), 506–515.

Ducros, Frédéric, Comte, Pierre & Lesieur, Marcel 1996 Large-eddy simulation of transition to turbulence in a boundary layer developing spatially over a flat plate. *J. Fluid Mech.* **326**, 1–36.

van Esch, B. P. M. 2009 Performance and radial loading of a mixed-flow pump under non-uniform suction flow. *ASME J. Fluids Eng.* **131** (5), 051101.

Feng, Jianjun, Benra, F. K. & Dohmen, H. J. 2009*a* Comparison of periodic flow fields in a radial pump among cfd, piv, and ldv results. *Int. J. Rotating Mach.* **2009**, 1–10.

Feng, Jianjun, Benra, F. K. & Dohmen, H. J. 2009*b* Unsteady flow visualization at part-load conditions of a radial diffuser pump: by piv and cfd. *J. Vis.* **12** (1), 65–72.

Feng, J., Benra, F. K. & Dohmen, H. J. 2011 Investigation of periodically unsteady flow in a radial pump by cfd simulations and ldv measurements. *ASME J. Turbomach.* **133** (1), 011004.

Gao, B., Guo, P. G., Zhang, N., Li, Z. & Yang, M. G. 2017 Unsteady pressure pulsation measurements and analysis of a low specific speed centrifugal pump. *ASME J. Fluids Eng.* **139** (7), 071101.

González, José, Fernández, Joaquín, Blanco, Eduardo & Santolaria, Carlos 2002 Numerical simulation of the dynamic effects due to

impeller-volute interaction in a centrifugal pump. *ASME J. Fluids Eng.* **124** (2), 348–355.

González, José, Parrondo, Jorge, Santolaria, Carlos & Blanco, Eduardo 2006 Steady and unsteady radial forces for a centrifugal pump with impeller to tongue gap variation. *ASME J. Fluids Eng.* **128** (3), 454–462.

Greitzer, E. M., Tan, C. S. & Graf, M. B. 2004 *Internal Flow: Concepts and Applications*. Cambridge University Press.

Gülich, Johann Friedrich 2008 *Centrifugal Pumps*, 1st edn. Springer-Verlag Berlin Heidelberg.

Hussain, A. K. M. F. & Reynolds, W. C. 1970 The mechanics of an organized wave in turbulent shear flow. *J. Fluid Mech.* **41** (2), 241–258.

Iaccarino, G., Ooi, A., Durbin, P. A. & Behnia, M. 2003 Reynolds averaged simulation of unsteady separated flow. *Int. J. Heat Fluid Flow* **24** (2), 147–156.

Jeong, J. & Hussain, F. 1995 On the identification of a vortex. *J. Fluid Mech.* **285**, 69–94.

Kato, Chisachi, Mukai, Hiroshi & Manabe, Akira 2003 Large-eddy simulation of unsteady flow in a mixed-flow pump. *Int. J. Rotating Mach.* **9** (5), 345–351.

Kim, Dokyun & Choi, Haecheon 2006 Immersed boundary method for flow around an arbitrarily moving body. *J. Comput. Phys.* **212** (2), 662–680.

Kim, Jungwoo, Kim, Dongjoo & Choi, Haecheon 2001 An immersed-boundary finite-volume method for simulations of flow in complex geometries. *J. Comput. Phys.* **171** (1), 132–150.

Kumar, Praveen & Mahesh, Krishnan 2017 Large eddy simulation of propeller wake instabilities. *J. Fluid Mech.* **814**, 361–396.

Kye, Beomjun, Park, Keuntae, Choi, Haecheon, Lee, Myungsung & Kim, Joo-Han 2018 Flow characteristics in a volute-type centrifugal pump using large eddy simulation. *Int. J. Heat Fluid Flow* **72**, 52–60.

Lee, Jungil, Choi, Haecheon & Park, Noma 2010 Dynamic global model for large eddy simulation of transient flow. *Phys. Fluids* **22** (7), 075106.

Lei, Cao, Yiyang, Zhang, Zhengwei, Wang, Yexiang, Xiao & Ruixiang, Liu 2015 Effect of axial clearance on the efficiency of a shrouded centrifugal pump. *ASME J. Fluids Eng.* **137** (7), 071101.

Lucius, A. & Brenner, G. 2010 Unsteady cfd simulations of a pump in part load conditions using scale-adaptive simulation. *Int. J. Heat Fluid Flow* **31** (6), 1113–1118.

Majidi, Kitano 2005 Numerical study of unsteady flow in a centrifugal pump. *ASME J. Turbomach.* **127** (2), 363–371.

Menter, F. R. 1994 Two-equation eddy-viscosity turbulence models for engineering applications. *AIAA J.* **32** (8), 1598–1605.

Nagahara, Takahide, Inoue, Yasuhiro, Sato, Toshiyuki, Sakata, Shinji, Nishimura, Kazumi & Kato, Chisachi 2005 Investigation of the flow field in a multistage pump by using les. In *Proceedings of FEDSM2005*.

Nicoud, F. & Ducros, F. 1999 Subgrid-scale stress modelling based on the square of the velocity gradient tensor. *Flow, Turbul. Combust.* **62**, 183–200.

Paone, N., Riethmuller, M. L. & Vandenbraembussche, R. A. 1989 Experimental investigation of the flow in the vaneless diffuser of a centrifugal pump by particle image displacement velocimetry. *Exp. Fluids* **7** (6), 371–378.

Park, Keuntae, Choi, Haecheon, Choi, Seokho & Sa, Yongcheol 2019 Effect of a casing fence on the tip-leakage flow of an axial flow fan. *Int. J. Heat Fluid Flow* **77**, 157–170.

Park, Noma, Lee, Sungwon, Lee, Jungil & Choi, Haecheon 2006 A dynamic subgrid-scale eddy viscosity model with a global model coefficient. *Phys. Fluids* **18** (12), 125109.

Parrondo, Jorge L., Gonza´lez-Pe´rez, Jose´ & Ferna´ndez-

Francos, Joaqui´n 2002 The effect of the operating point on the pressure fluctuations at the blade passage frequency in the volute of a centrifugal pump. *ASME J. Fluids Eng.* **124** (3), 784–790.

Pedersen, N., Larsen, P. S. & Jacobsen, C. B. 2003 Flow in a centrifugal pump impeller at design and off-design conditions - part i: Particle image velocimetry (piv) and laser doppler velocimetry (ldv) measurements. *ASME J. Fluids Eng.* **125** (1), 61–72.

Piomelli, Ugo & Liu, Junhui 1995 Large-eddy simulation of rotating channel flows using a localized dynamic model. *Phys. Fluids* **7** (4), 839–848.

Posa, Antonio 2021 Les investigation on the dependence of the flow through a centrifugal pump on the diffuser geometry. *Int. J. Heat Fluid Flow* **87**, 108750.

Posa, Antonio & Lippolis, Antonio 2018 A les investigation of off-design performance of a centrifugal pump with variable-geometry diffuser. *Int. J. Heat Fluid Flow* **70**, 299–314.

Posa, Antonio & Lippolis, Antonio 2019 Effect of working conditions and diffuser setting angle on pressure fluctuations within a centrifugal pump. *Int. J. Heat Fluid Flow* **75**, 44–60.

Posa, Antonio, Lippolis, Antonio & Balaras, Elias 2015 Large-eddy simulation of a mixed-flow pump at off-design conditions. *ASME J. Fluids Eng.* **137** (10), 101302.

Posa, Antonio, Lippolis, Antonio & Balaras, Elias 2016 Investigation of separation phenomena in a radial pump at reduced flow rate by large-eddy simulation. *ASME J. Fluids Eng.* **138** (12), 121101.

Posa, Antonio, Lippolis, Antonio, Verzicco, Roberto & Balaras, Elias 2011 Large-eddy simulations in mixed-flow pumps using an immersed-boundary method. *Comput. Fluids* **47** (1), 33–43.

Reeves, David T. 2001 Study on improving the energy efficiency of pumps. *Tech. Rep.* AEAT-6559. European Commission.

Reynolds, W. C. & Hussain, A. K. M. F. 1972 The mechanics of an orga-

nized wave in turbulent shear flow. part 3. theoretical models and comparisons with experiments. *J. Fluid Mech.* **54** (2), 263–288.

Shi, F.and Tsukamoto, H. 2001 Numerical study of pressure fluctuations caused by impeller-diffuser interaction in a diffuser pump stage. *ASME J. Fluids Eng.* **123** (3), 466–474.

Shimada, K. & Ishihara, T. 2002 Application of a modified k–$\boldsymbol{\varepsilon}$ model to the prediction of aerodynamic characteristics of rectangular cross-section cylinders. *J. Fluids Struct.* **16** (4), 465–485.

Smagorinsky, J. 1963 General circulation experiments with the primitive equations. *Monthly Weather Review* **91** (3), 99–164.

Spence, R. & Amaral-Teixeira, J. 2009 A cfd parametric study of geometrical variations on the pressure pulsations and performance characteristics of a centrifugal pump. *Comput. Fluids* **38** (6), 1243–1257.

Stel, H., Amaral, G. D. L., Negrão, C. O. R., Chiva, S., Estevam, V. & Morales, R. E. M. 2013 Numerical analysis of the fluid flow in the first stage of a two-stage centrifugal pump with a vaned diffuser. *ASME J. Fluids Eng.* **135** (7), 071104.

Strelets, M. 2001 Detached eddy simulation of massively separated flows. In *AIAA Aerosp. Sci. Meet. Exhib., 39th*.

Tan, Lei, Zhu, Baoshan, Wang, Yuchuan, Cao, Shuliang & Gui, Shaobo 2015 Numerical study on characteristics of unsteady flow in a centrifugal pump volute at partial load condition. *Eng. Comput.* **32** (6), 1549–1566.

Torner, Benjamin, Hallier, Sebastian, Witte, Matthias & Wurm, Frank-Hendrik 2017 Large-eddy and unsteady reynolds-averaged navier-stokes simulations of an axial flow pump for cardiac support. In *Proceedings of ASME 2017 Turbo Expo: Turbomachinery Technical Conference and Exposition*.

Ubaldi, M., Zunino, P. & Ghiglione, A. 1998 Detailed flow measurements

within the impeller and the vaneless diffuser of a centrifugal turbomachine. *Exp. Therm. Fluid Sci.* **17**, 147–155.

Yan, Peng, Chu, Ning, Wu, Dazhuan, Cao, Linlin, Yang, Shuai & Wu, Peng 2017 Computational fluid dynamics-based pump redesign to improve efficiency and decrease unsteady radial forces. *ASME J. Fluids Eng.* **139** (1), 011101.

Zhang, Ning, Liu, Xiaokai, Gao, Bo, Wang, Xiaojun & Xia, Bin 2019 Effects of modifying the blade trailing edge profile on unsteady pressure pulsations and flow structures in a centrifugal pump. *Int. J. Heat Fluid Flow* **75**, 227–238.

Zhang, Ning, Yang, Minguan, Gao, Bo, Li, Zhong & Ni, Dan 2016 Investigation of rotor-stator interaction and flow unsteadiness in a low specific speed centrifugal pump. *Strojniški vestnik - Journal of Mechanical Engineering* **62** (1), 21–31.

Appendix A

Modified volute casing to reduce the leakage to cavities

As investigated earlier, axial pressure gradient in the volute especially near the tongue induce strong leakage to top and bottom cavities. This generates significant losses and decreases pump efficiency. The present pump has large cavity area and suffers from substantial leakages especially at the off-design condition (part I). The axial clearances of top and bottom cavities for the present pump are much larger than the one proposed by Gülich (2008), which is from $0.03R_2$ to $0.08R_2$. Lei *et al.* (2015) considered even smaller clearances from $0.001R_2$ to $0.005R_2$ reporting that pump with smaller clearance shows higher pump efficiency.

In the present study, we modify the volute casing by reducing cavity area between the impeller and volute casing to increase the pump efficiency. Figure A.1 shows the schematic diagram of the base pump and modified pump with smaller cavity area. The axial clearances of the top and bottom cavity are designed to be about $0.02R_2$ and $0.03R_2$, respectively. These are adopted considering both hydrodynamic efficiency and

mechanical design. Figure A.2 shows the magnitude of the instantaneous cross flow velocity at the off-design condition on x-r plane at 5° ahead of the volute tongue. Considerable leakages to top and bottom cavities occur in the base pump, whereas those are notably weakened in the modified pump. The pump efficiency is increased by 4.4% and 6.7% at design and off-design conditions, respectively. The increase in pump efficiency is larger for the off-design condition than for the design condition because of larger leakage at the former condition.

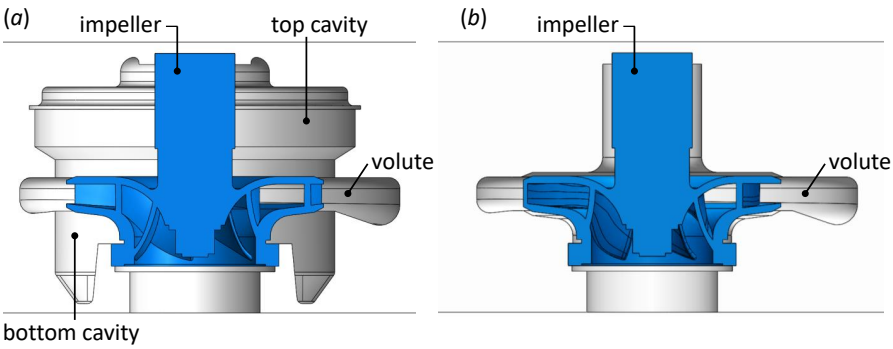

Figure A.1: Schematic diagram of the base pump and the modified pump: (a) base pump; (b) modified pump

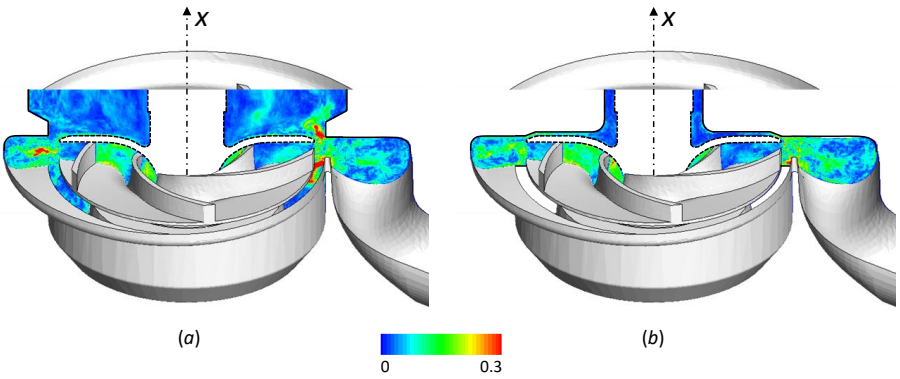

Figure A.2: Contours of the cross flow velocity magnitude at the off-design condition on x-r plane at 5° ahead of the volute tongue: (a) base pump; (b) modified pump

Appendix B

Circumferential grooves to reduce the leakage to the pump inlet

As examined so far, leakage produces considerable losses in a pump. Especially, part of leakage to bottom cavity travels to the pump inlet through the wear-ring clearance between the impeller and volute casing. In this section, we consider the wear-ring clearance and leakage to the pump inlet. Figure B.1 shows the schematic diagram of pump with two different wear-ring clearances. To reduce the leakage to the pump inlet through the wear-ring clearance, we apply circumferential grooves as in figure B.1(b).

Due to the pressure difference between the bottom cavity and pump inlet, the pump with the original wear-ring clearance suffers from substantial leakage by about 6.7% and 12% at design and off-design conditions, respectively. This is shown in figure B.2(a). The leakage has azimuthal velocity due to the impeller's rotation. The circumferential grooves obstruct the flow through the wear-ring clearance decreasing the amount of leakage. Consequently, leakage to the pump inlet diminishes to about 3.7% and 6.9% at design and off-design conditions, respectively. This is

approximately half of leakage through the original wear-ring clearance. Consequently, the circumferential grooves improve the pump efficiency by about 2.5% and 2.3% at design and off-design conditions, respectively. Together with the modified pump with reduced cavity in appendix A, we could improve the pump efficiency by approximately 7.0% and 9.2% at design and off-design conditions, respectively.

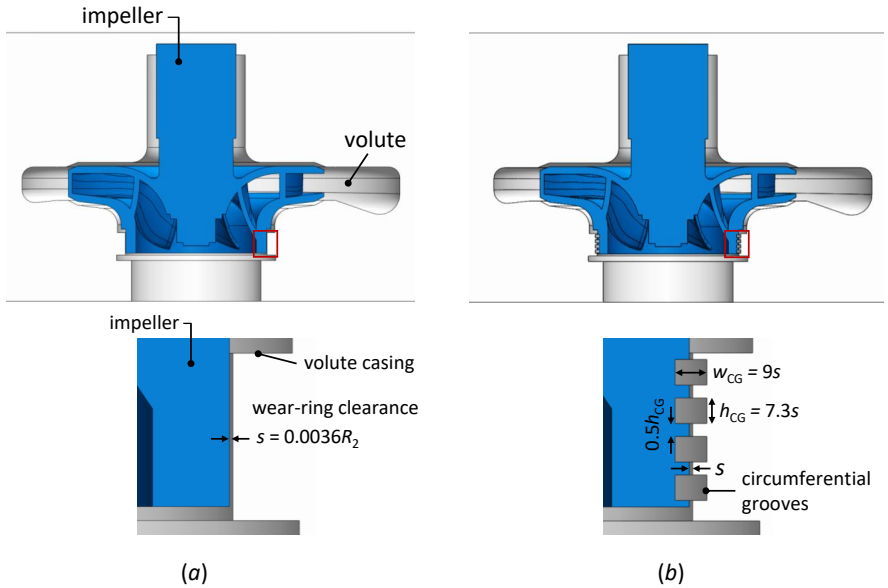

Figure B.1: Schematic diagram of pumps with two different wear-ring clearances: (a) the original wear-ring clearance; (b) the wear-ring clearance with circumferential grooves

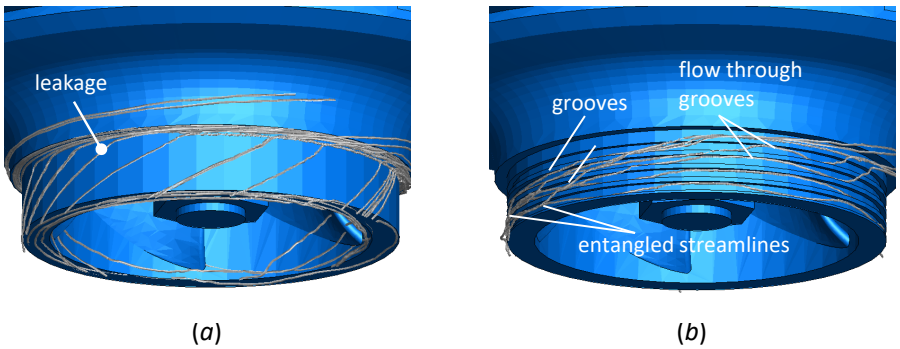

Figure B.2: Instantaneous streamlines through wear-ring clearances: (a) the original wear-ring clearance; (b) the wear-ring clearance with circumferential grooves

LES 및 URANS를 이용한 원심펌프 내부의 난류 유동해석

서울대학교 대학원
기계항공공학부
계 범 준

요 약

원심펌프는 가장 널리 이용되는 펌프로서 저압에서 다양한 산업 분야에서 많은 유량을 이송하기 위해 사용되고 있다. 원심펌프는 다양한 범위의 압력 상승 및 유량 조건을 만족하기 위해 설계 조건뿐 아니라 탈설계 조건에서도 흔히 작동한다. 탈설계 조건에서는 펌프 내부에서 더 복잡한 난류 유동 특성이 발달하여 널리 사용되는 비정상 Reynolds 평균 Navier-Stokes 난류 모델(unsteady Reyonolds Navier-Stokes: URANS)가 부정확한 결과를 도출할 수 있다는 것이 잘 알려져 있다. 따라서 이러한 탈설계 조건 해석을 위해서는 큰에디모사(large eddy simulation: LES)와 같은 보다 정확한 수치해석 방법이 요구된다.

1장에서는 원심펌프 내부 난류 유동 해석을 위해 LES를 수행하고 설계 조건 및 탈설계 조건에서의 유동 특성을 분석하였다. 임펠러 블레이드의 압

력 및 흡입면 모두에서 유동 박리가 발생하였고, 특히 탈설계 조건에서는 블레이드 압력면의 박리 기포가 비정상 특성을 나타내며 볼루트 혀 부근에서 더 크게 발달하였다. 블레이드 회전에 따라 블레이드 후단으로부터 와류 구조가 발생하였고 탈설계 조건에서는 이들이 다음 블레이드 후단 와류와 강하게 상호 작용하여 볼루트 내부에서 더 강한 와도장을 생성하였다. 임펠러 주변 압력 섭동을 살펴보기 위해서 삼중 분해를 수행하였다. 압력의 난류 섭동은 볼루트 혀 부근에서 크게 증가하였고 특히 탈설계 조건에서는 주기적 섭동보다 강하게 발달하였다. 볼루트 혀에서는 유동 박리가 발생하였다. 특히 탈설계 조건에서는 많은 유량이 출구 파이프로 흐르지 않고 임펠러-볼루트 간극을 따라 볼루트 상류로 누설되었다. 이는 블레이드 압력면에 강한 역압력 구배를 형상하여 박리기포의 재부착을 지연시키고 비정상적인 유동박리 현상을 생성하였다. 또한 볼루트에서의 높은 압력은 축 방향으로의 압력 구배를 형성하고 반경 방향 간극으로 누설 유동을 야기하였다. 탈설계 조건에서는 볼루트 내부에서 더 높은 압력이 형성되어 누설 유동이 강하게 발달하며 볼루트 내부에서의 이차 유동의 발달에 기여하였다. 이러한 원심펌프 내부의 다양한 손실유동은 임펠러-볼루트 상호작용에 의해 영향을 받아 탈설계 조건에서 더 크게 발달하였다.

2장에서는 URANS 해석을 수행하고 이를 LES에서의 유동 특성과 비교하였다. LES는 두 유량 조건에서 펌프의 압력 상승 및 효율을 잘 예측하였지만, URANS는 이들을 과다 예측하였다. URANS의 블레이드 후단 와류 구조는 LES의 순간 유동 구조를 잘 나타내지 못 하였고, 오히려 LES의 상평균 유동 구조와 유사한 와도장을 나타내었다. 설계점에서 LES 및 URANS는 블레이드 표면을 따라 유사한 압력 및 마찰항력 분포를 나타내었다. 하지만 탈설계점에서 LES는 볼루트 혀 부근 블레이드 압력면을 따라 박리기포의 재부착이 지연되어 더 큰 박리기포가 형성되었는데, URANS는 이를 예측하지 못 하였다. 임펠러 주변에서의 압력 섭동은 URANS가 주기적 섭동 성분은 비교적 잘 예측하지만, 난류 섭동을 잘 예측하지 못 하는

것을 보여주었다. 따라서 난류 섭동이 중요해지는 탈설계점에서는 URANS를 통한 압력 섭동 예측이 부정확한 결과를 나타내었다. 또한 설계점에서는 LES 및 URANS가 볼루트 내부를 따라 유사한 전압 분포를 나타내었다. 하지만 탈설계점에서는 볼루트 혀에서 발생하는 유동박리가 손실을 야기하고 볼루트 상류에서 전압이 크게 감소하였다. URANS는 이러한 손실을 잘 예측하지 못 하였지만 이외 영역에서는 전압 분포를 잘 예측하였다. 또한 본 연구에서의 펌프에서는 토출 파이프의 곡률 및 면적 증가로 인해 강한 와류 유동이 발생하였다. 이러한 와류 유동은 큰 손실을 야기하고 이는 설계 조건에서 높은 유량으로 인해 더 크게 발달하였다. LES는 이러한 와류 유동 및 손실을 잘 예측하여 실험에서의 압력 상승 및 효율을 잘 예측하였지만, URANS는 이를 예측하지 못 하여 펌프 성능을 과다예측하였다.

주요어: 원심펌프, 임펠러-볼루트 상호작용, 큰 에디모사(LES), 비정상 Navier-Stokes 방정식 해석(URANS), LES 및 URANS 비교

학 번: 2015-22698

감사의 글

2015년 여름, 좋은 연구를 하고 싶다는 꿈을 품고 연구실에 온 때가 기억이 납니다. 처음에는 수치 기법, 코드 공부를 하는 것만으로도 즐거웠고 훌륭한 연구자가 되고자 하는 의지도 더 충만했던 것 같습니다. 그때의 초심을 잃지 않고 더 열심히 했다면 좋았겠다는 아쉬움도 남지만, 부족한 제가 무사히 학위 과정을 마칠 수 있었던 것은 교수님을 비롯하여 여러 선후배 분들의 도움이 있었기 때문입니다.

먼저 지도교수님이신 최해천 교수님께 감사의 말씀을 드리고 싶습니다. 처음 교수님과 면담을 할 때, 적지 않은 나이로 학위과정을 시작하려고 하는 저를 교수님께서 과연 받아주실까 하는 걱정이 있었습니다. 걱정이 무색하게도 교수님께서는 연구를 하고 싶다고 찾아온 학생은 언제나 받아주시겠다고 하시며 격려를 해주셨습니다. 한평생의 열정적인 연구자의 모습, 유쾌함을 잃지 않으시면서도 필요할 때는 엄격하신 모습, 좋은 발표와 논문을 완성하기 위한 세세함 등 많은 부분에서 감명을 받았고 무엇보다도 independent researcher가 되기 위한 지도와 격려를 아낌없이 주신 점에 감사드립니다.

항상 제 버팀목이 되어 주는 부모님과 동생에게도 감사를 전합니다. 다른 사람들보다 늦은 나이에 하고 싶은 연구를 마음껏 할 수 있었던 것은 큰 축복이고, 가족들의 지지가 큰 힘이 되었습니다. 항상 제게 큰 의지와 위로가 되었던 할머니 및 친척 분들에게도 감사를 드립니다. 할머니께서 돌아가시기 전에 박사 학위 받는 모습을 보여드리고 싶었는데 죄송하고 그간 저에 대한 응원과 기도에 감사드립니다.

연구실 생활을 같이 한 소중한 선후배 분들에게도 깊은 감사드립니다. 무엇보다도 제 연구를 본인 연구처럼 깊이 고민하고 큰 도움을 준 근태 형에게 진심으로 감사드립니다. 또한 같이 과제를 하면서 고생이 많았던 원혁이에게도 고맙다는 말을 전하고 싶습니다. 연구실을 떠나 각자의 분야에서 훌륭히 맡은 바를 다 하고 있는 김주하 교수님, 태용이 형, 인재 형, 우진이 형, 현식이 형, 홍권이 형, 희수 형, 승현이 형, 민희 누나, 창우, 한별, 세형, 민정, 경태, 기영, 재림, 동리,

소희, 문흠, 종현, 형민, 규태, 지유, 승영, 한솔, 소민, 은섭에게 감사드리고 항상 행운이 가득하기를 바랍니다. 연구실에서 훌륭한 연구를 계속하고 있는 성현이 형, 도현, 종환, 재희, 영진, 인구, 상우, 종헌, 현우, 다은, 명화, 종혁, 혁수, 혜정, Wu Zhi의 앞날에 훌륭한 성과가 함께 하기를 바랍니다. 안타까운 사고로 세상을 떠난 준영의 명복을 바라고, 연구실 생활을 하는데 큰 도움을 준 허강은, 홍연화, 서명희 씨에게도 감사드립니다.

박사논문 심사를 허락해 주시고 연구를 발전시킬 수 있도록 조언을 아끼지 않으신 송성진, 황원태, 이창훈, 이정일 교수님들께도 감사의 인사를 전합니다. 제 연구에 큰 도움을 주신 한국전자기술연구원의 김주한, 이명성 박사님, 두크펌프의 윤인식 소장님, 조민태 박사님 등의 관계자 분들께도 감사드립니다. 특히 이명성 박사님의 관심과 응원이 큰 힘이 되었습니다. 이외에도 제가 미처 기억하지 못하고 언급하지 못하였지만 격려와 도움 주신 모든 분들께 감사를 드립니다.

마지막으로 제 대학원 생활을 함께하고 앞으로의 미래를 같이 그려갈 사랑하는 아내 주혜에게 고맙습니다. 6년간의 학위 과정을 무사히 마칠 수 있었던 가장 큰 공헌자는 아내입니다. 누구 말마따나 제 대학원 생활에서의 가장 큰 결실은 인생의 반려자인 아내를 만난 것이 아닐까 합니다. 장인어른, 장모님, 명신 누님, 흥식 형님, 미령 누님, 앨런, 소봉이에게도 감사를 드리고 앞으로 항상 건강하고 행복하길 바라겠습니다.

소중한 인연이 되어주신 모든 분들께 감사한 마음을 시 한 편에 담아 전합니다.

계범준 드림

함께 있으면 좋은 사람

용혜원

그대를 만나던 날
느낌이 참 좋았습니다
착한 눈빛, 해맑은 웃음
한마디, 한 마디의 말에도
따뜻한 배려가 있어
잠시 동안 함께 있었는데
오래 사귄 친구처럼
마음이 편안했습니다

내가 하는 말들을
웃는 얼굴로 잘 들어주고
어떤 격식이나 체면 차림 없이
있는 그대로를 보여주는
솔직하고 담백함이
참으로 좋았습니다.

그대가 내 마음을 읽어주는 것만 같아
둥지를 잃은 새가
새 둥지를 찾은 것만 같았습니다
짧은 만남이지만
기쁘고 즐거웠습니다

오랜만에 마음을 함께
맞추고 싶은 사람을 만났습니다
마치 사랑하는 사람에게
장미꽃 한 다발을 받은 것보다
더 행복했습니다

그대는 함께 있으면 있을수록
더 좋은 사람입니다